Quaternary Science Reviews 257 (2021) 106842

Contents lists available at ScienceDirect

Quaternary Science Reviews

journal homepage: www.elsevier.com/locate/quascirev

New insights from multi-proxy data from the West Antarctic continental rise: Implications for dating and interpreting Late Quaternary palaeoenvironmental records

C.-D. Hillenbrand [a, *], S.J. Crowhurst [b], M. Williams [a], D.A. Hodell [b], I.N. McCave [b], W. Ehrmann [c], C. Xuan [d], A.M. Piotrowski [b], F.J. Hernández-Molina [e], A.G.C. Graham [f, g], H. Grobe [h], T.J. Williams [a, b, i], J.R. Horrocks [j], C.S. Allen [a], R.D. Larter [a]

[a] British Antarctic Survey, High Cross, Madingley Road, Cambridge, CB3 0ET, UK
[b] Department of Earth Sciences, University of Cambridge, Downing Street, Cambridge, CB2 3EQ, UK
[c] Institute for Geophysics and Geology, University of Leipzig, Talstrasse 35, Leipzig, 04103, Germany
[d] School of Ocean and Earth Science, National Oceanography Centre Southampton, University of Southampton, Waterfront Campus, European Way, Southampton, SO14 3ZH, UK
[e] Department of Earth Sciences, Royal Holloway University of London, Egham, Surrey, TW20 0EX, UK
[f] College of Life and Environmental Sciences, University of Exeter, Exeter, EX4 4RJ, UK
[g] College of Marine Science, University of South Florida, St Petersburg, FL, USA
[h] Alfred-Wegener-Institut Helmholtz-Zentrum für Polar- und Meeresforschung, Bremerhaven, Germany
[i] Department of Geological Sciences, University of Florida, Gainesville, FL, USA
[j] Department of Geography, Durham University, Durham, DH1 3LE, UK

ARTICLE INFO

Article history:
Received 23 August 2020
Received in revised form
24 January 2021
Accepted 4 February 2021
Available online 24 February 2021

Handling Editor: C. O'Cofaigh

Keywords:
Antarctic Peninsula
Bioturbation
Bottom current
Carbon burn-down
Contourites
Ice-rafted debris
Manganese enrichment
Non-steady-state diagenesis
Sediment drifts

ABSTRACT

The Antarctic Peninsula's Pacific margin is one of the best studied sectors of the Antarctic continental margin. Since the 1990s, several research cruises have targeted the continental rise with geophysical surveys, conventional coring and deep-sea drilling. The previous studies highlighted the potential of large sediment drifts on the rise as high-resolution palaeoenvironmental archives. However, these studies also suffered from chronological difficulties arising from the lack of calcareous microfossils, with initial results from geomagnetic relative palaeointensity (RPI) dating promising a possible solution.

This paper presents data from new sediment cores recovered on cruise JR298 from seven continental rise sites west of the Antarctic Peninsula and in the Bellingshausen Sea with the objectives to (i) seek calcareous foraminifera, especially at shallow drift sites, to constrain RPI-based age models, and (ii) investigate the depositional history at these locations. We present the results of chronological and multi-proxy analyses on these cores and two cores previously collected from the study area. We establish new age models for the JR298 records and compare them with published RPI-based age models. In addition, we evaluate the reliability of different palaeoproductivity proxies and infer depositional processes.

Planktic foraminifera are present in various core intervals. Although their stable oxygen isotope ($\delta^{18}O$) ratios, tephrochronological constraints and glacial-interglacial changes in sediment composition provide age models largely consistent with the RPI chronologies, we also observe distinct differences, predominantly in the Bellingshausen Sea cores. Enrichments of solid-phase manganese together with evidence for "burn-down" of organic carbon in late glacial and peak interglacial sediments document non-steady-state diagenesis that may have altered magnetic mineralogy and, thus, RPI proxies. This process may explain discrepancies between RPI-based age models and those derived from $\delta^{18}O$ data combined with tephrochronology. The data also indicate that organic carbon is a much less reliable productivity proxy than biogenic barium or organically-associated bromine in the investigated sediments.

In agreement with previous studies, sediment facies indicate a strong control of deposition on the rise by bottom currents that interacted with detritus supplied by meltwater plumes, gravitational down-slope transport processes and pelagic settling of iceberg-rafted debris (IRD) and planktic microfossils. Bottom-current velocities underwent only minor changes over glacial-interglacial cycles at the drift crests, with down-slope deposition only rarely affecting these shallow locations. Maximum

* Corresponding author.
E-mail address: hilc@bas.ac.uk (C.-D. Hillenbrand).

https://doi.org/10.1016/j.quascirev.2021.106842

concentrations of coarse IRD at the seafloor surfaces of the shallow sites result predominantly from upward pumping caused by extensive bioturbation. This process has to be taken into account when past changes in IRD deposition are inferred from quantifying clasts >1 mm in size.

1. Introduction

The western continental rise of the Antarctic Peninsula is characterized by eight large and four smaller mounds rising between several hundred and ≤2000 m above the surrounding seafloor (Fig. 1; Rebesco et al., 2002; Hillenbrand et al., 2008b; Hernández-Molina et al., 2017). The mounds are separated by deep-sea channels originating at the base of the continental slope, and usually have a gentle NE side and a steep SW flank. They are interpreted as contourite mounded drifts formed by fine-grained detritus, which initially had been supplied by turbidity currents travelling through the channels before the fine-grained particles were entrained into a generally SW-ward flowing bottom current (Rebesco et al., 1997) [NB: here we use the term "contourite" *sensu lato*, i.e., as describing any sediment deposited or reworked by a bottom current (e.g., Rebesco et al., 2014; Stow and Smillie 2020)]. The bottom current follows the bathymetric contours and originates as highly modified Weddell Sea Deep Water (WSDW) or Lower Circumpolar Deep Water (LCDW) from the Weddell Sea (Camerlenghi et al., 1997; Giorgetti et al., 2003). The drifts were examined with high-resolution bathymetric surveys (Rebesco et al. 2002, 2007; Dowdeswell et al., 2004; Larter et al., 2016), reflection seismic investigations (Larter and Cunningham 1993; McGinnis et al., 1997; Rebesco et al. 1997, 2002; Hernández-Molina et al., 2017) and shallow gravity and piston coring (Pudsey and Camerlenghi 1998; Pudsey 2000; Lucchi et al., 2002; Vautravers et al., 2013). In addition, Drifts 7 and 4 were drilled at Sites 1095, 1096 and 1101 by Ocean Drilling Program (ODP) Leg 178 (Barker et al. 1999, 2002).

Further west, the continental margin in the Bellingshausen Sea has been only sparsely studied by a few high-resolution bathymetric lines and seismic profiles. These surveys identified the Belgica Trough Mouth Fan ('Belgica TMF'; Dowdeswell et al., 2008) and one major sediment drift (Nitsche et al., 2000; Cunningham et al., 2002). In contrast to the Antarctic Peninsula rise, data from only two marine sediment cores have been published from the continental rise in the Bellingshausen Sea (Fig. 1; PS2538, Hillenbrand et al., 2005; PS2556, Hillenbrand et al., 2008a).

Multi-proxy analyses of the cores from the Antarctic Peninsula margin revealed that the drifts contain records of Late Neogene to Quaternary palaeoenvironmental changes, including past dynamics of the Antarctic Peninsula Ice Sheet (APIS) and oceanographic variability in the Antarctic Zone of the Southern Ocean (e.g., Pudsey 2000; Lucchi et al., 2002; Barker et al., 2002; Hillenbrand and Ehrmann 2005; Bart et al., 2007; Cowan et al., 2008; Hepp et al., 2009; Escutia et al., 2009). The rarity of calcareous microfossils in the predominantly terrigenous drift sediments prevented reliable AMS ^{14}C dating and the application of stable oxygen isotope (δ^{18}O) stratigraphy; the cores could only be dated by lower-resolution bio-, magneto- and lithostratigraphy (Pudsey and Camerlenghi 1998; Pudsey 2000; Barker et al., 2002; Lucchi et al., 2002). This difficulty hampered high-resolution reconstructions and thus full exploitation of the drift archives. Nevertheless, establishing age models for the drift cores by correlating reconstructions of relative palaeointensity (RPI) with independently dated regional/global RPI records has shown some promise (Guyodo et al., 2001; Sagnotti et al., 2001; Macrì et al., 2006; Venuti et al., 2011; Vautravers et al., 2013).

International Ocean Discovery Program (IODP) proposal 732-FULL2 (Channell et al., 2008) advocated the recovery of new drill cores from the western Antarctic Peninsula and the Bellingshausen Sea rise. Its primary objective is to fully exploit the drifts' palaeoarchives for reconstructing Miocene to Holocene oceanographic changes in the eastern Pacific sector of the Southern Ocean and the dynamics of the APIS and the marine based West Antarctic Ice Sheet (WAIS). The main strategy is to obtain continuous records from shallow drift crest sites, where both accumulation rates and the preservation potential of calcareous foraminifera are expected to be high, in order to establish reliable, high-resolution age models using RPI proxies constrained by foraminiferal δ^{18}O stratigraphy.

Here, we present multi-proxy data sets from sediment cores recovered from the West Antarctic margin during pre-site survey cruise JR298 in support of IODP proposal 732-FULL2 and two additional cores collected on earlier research cruises. The RPI records of the JR298 cores were recently published by Channell et al. (2019). Here, we present the sedimentological data sets, including proxy measurements, which previously had not - or only to a very limited extent - been carried out on cores from the area, such as sortable silt mean size ($\overline{SS}$) analyses and X-ray fluorescence (XRF) scanning. We focus our discussion on novel findings from these investigations.

2. Materials and methods

2.1. Materials

Seven piston cores (PC) were recovered on cruise JR298 of the RRS *James Clark Ross* in 2015 (Table 1). Six PCs targeted drill sites of IODP proposal 732-FULL2 (Channell et al., 2008), i.e. the shallowest parts of Drifts 4, 5, 6 and 7 on the western Antarctic Peninsula rise, the Bellingshausen Sea drift, and the distal part of Belgica TMF (Fig. 1). In addition, PC734 targeted the distal crest of Drift 5 to obtain a more condensed sedimentary sequence, and giant box core (GBC) GBC733 was retrieved from the channel separating Drifts 5 and 5A (Fig. 1). A GBC was deployed at each PC site to obtain undisturbed seafloor surface sediments. Data from GBC sub-cores and the corresponding PCs were spliced to compensate for sediment loss and/or possible core-top disturbance in the PCs. Overall, PC quality was excellent, with only minor core-top disturbance/sediment loss. However, X-radiographs revealed sediment inflow at the bases of several PCs. No data are presented from those core intervals. The PCs were sectioned and, together with the GBC sub-cores, split and sampled on board. All sections and samples were stored at +4 °C after collection.

We also present data from RV *Polarstern* gravity cores (GCs) PS1565-2 recovered from the seaward, distal flank of Drift 3 in 1987 and PS2556-2 [including multiple core (MUC) PS2556-1] collected from the crest of the Bellingshausen Sea drift in 1994 (Fig. 1; Table 1). Some data from cores PS1565-2 and PS2556-2/-1 were previously published (Hillenbrand and Ehrmann 2002; Hillenbrand et al., 2008a).

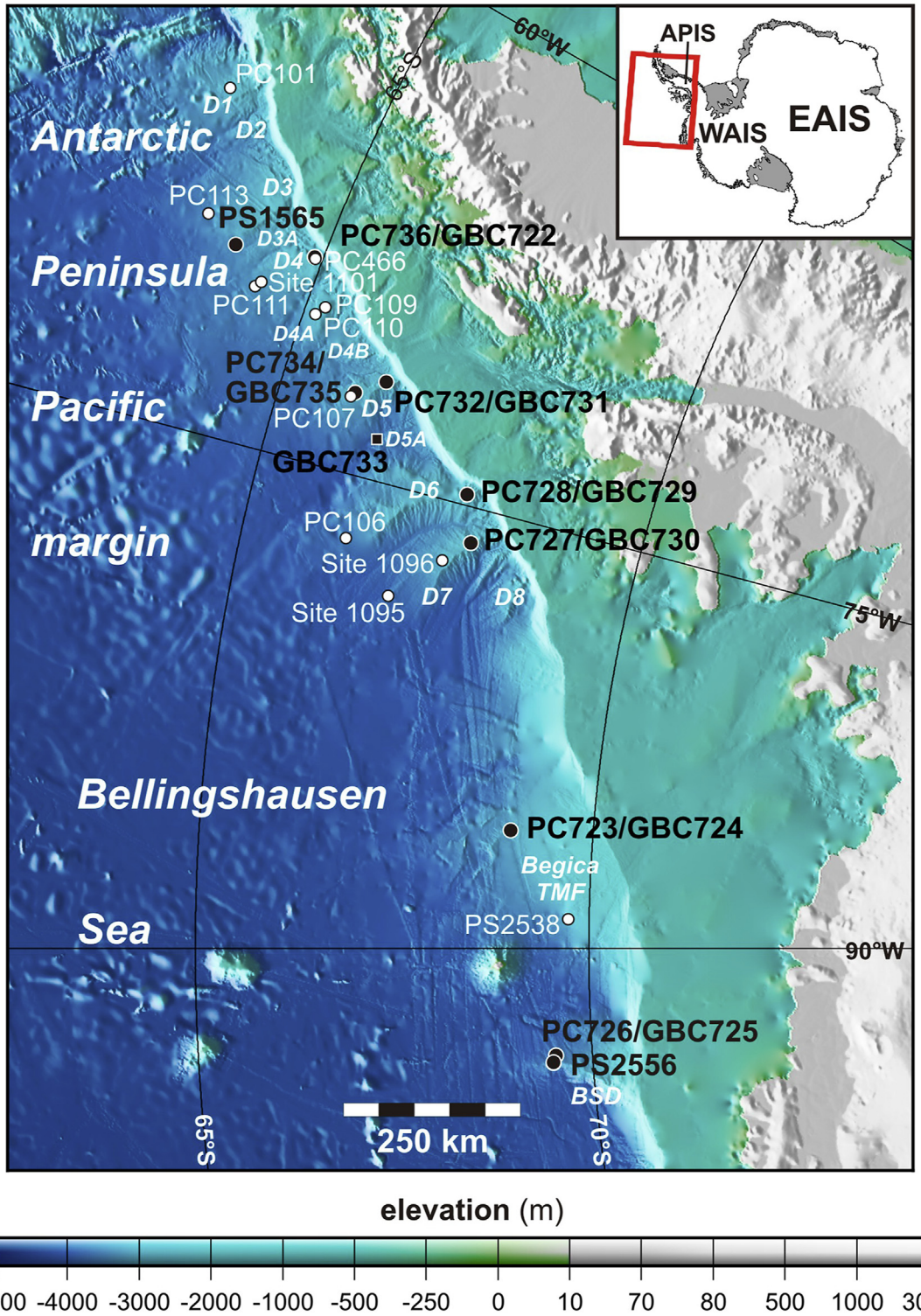

Fig. 1. Bathymetric map of the study area with locations of sediment cores analysed for this study (black symbols) and other core sites mentioned in the text (white dots). Numbering of the drifts west of the Antarctic Peninsula (*D1* to *D8*) follows Rebesco et al. (2002). Bathymetry is from IBCSO (Arndt et al., 2013). Belgica TMF: Belgica Trough Mouth Fan; BSD: Bellingshausen Sea Drift. Inset map shows study area within wider context of Antarctica. APIS: Antarctic Peninsula Ice Sheet; EAIS: East Antarctic Ice Sheet; WAIS: West Antarctic Ice Sheet.

2.2. Methods

Whole-core magnetic susceptibility (MS) was measured on the PC sections using a 120-mm diameter Bartington loop sensor (MS2C) connected to a Bartington MS3 susceptibility meter. After the splitting of the PC and GBC sections, their working and archive halves were photographed before the sediment lithology and structures were described visually and using smear slides. After cruise JR298, the core logs were refined/revised using X-radiographs prepared from the PC and GBC archive halves. P-wave

Table 1
Cruise, core ID, gear (GBC: giant box core, GC: gravity core, MUC: multiple core, PC: piston core), location (BS: Bellingshausen Sea; TMF: Trough Mouth Fan), latitude (Lat), longitude (Long), water depth (WD), and recovery (Rec) for the sediment cores investigated in this study. Where applicable, the IDs for sites of IODP proposal 732-FULL-2 (Channell et al., 2008) are given under "Location".

Cruise	Core ID	Gear	Location	Lat (°)	Long (°)	WD (m)	Rec (m)
JR298	GBC722	GBC	Proximal crest Drift 4 (PEN-1)	−64.8953	−69.0357	2329	0.37
JR298	PC723	PC	Toe of Belgica TMF (BELS-1)	−68.9428	−85.7903	3075	11.09
JR298	GBC724	GBC	Toe of Belgica TMF (BELS-1)	−68.9428	−85.7900	3073	0.41
JR298	GBC725	GBC	Crest BS drift (BELS-2C)	−69.5317	−93.9158	3660	0.47
JR298	PC726	PC	Crest BS drift (BELS-2C)	−69.5317	−93.9158	3663	12.00
JR298	PC727	PC	Proximal crest Drift 7 (PEN-4B)	−67.8643	−76.1793	2681	9.90
JR298	PC728	PC	Proximal crest Drift 6 (PEN-3B)	−67.6683	−74.6423	2454	12.17
JR298	GBC729	GBC	Proximal crest Drift 6 (PEN-3B)	−67.6683	−74.6430	2449	0.28
JR298	GBC730	GBC	Proximal crest Drift 7 (PEN-4B)	−67.8643	−76.1793	2680	0.335
JR298	GBC731	GBC	Proximal crest Drift 5 (PEN-2B)	−66.2722	−71.9089	2654	0.325
JR298	PC732	PC	Proximal crest Drift 5 (PEN-2B)	−66.2722	−71.9085	2647	9.40
JR298	GBC733	GBC	Channel between Drifts 5 & 5A	−66.3722	−73.7045	3857	0.28
JR298	PC734	PC	Crest Drift 5	−65.9382	−72.5175	3000	12.93
JR298	GBC735	GBC	Crest Drift 5	−65.9382	−72.5173	2998	0.34
JR298	PC736	PC	Proximal crest Drift 4 (PEN-1)	−64.8953	−69.0355	2325	10.255
ANT-XI/3	PS2556-1	MUC	Crest BS drift	−69.4983	−94.1683	3586	0.40
ANT-XI/3	PS2556-2	GC	Crest BS drift	−69.4933	−94.1583	3594	9.62
ANT-VI/2	PS1565-2	GC	Distal flank Drift 3	−63.9075	−69.5082	3427	11.71

velocity, MS and wet-bulk density (WBD) of the archive halves were analysed with a GEOTEK multi-sensor core logger (MSCL-S). Semi-quantitative elemental data and diffuse-reflectance spectrophotometric data were measured on the archive halves using a 3rd generation Avaatech XRF scanner. Elemental data are recalculated and plotted as log-normalised (LN) peak-area ratios (Weltje and Tjallingii, 2008) but in the following text we refer just to element ratios. Methodological details for the XRF scanning and magnetic investigations conducted on U-channels from the PCs and discrete bulk samples from the PCs and GBCs are given in Channell et al. (2019).

Discrete 1 cm thick bulk samples (~48 cm^3) were taken from the PC and GBC working halves for sedimentological, micropalaeontological, geochemical and mineralogical studies. The sampling intervals varied depending on the visually observed changes in lithology and sedimentary structures. Water content was determined by weighing the samples before and after oven drying at 30 °C. Grain-size distribution in terms of weight percentages of gravel (>2000 μm), sand (63–2000 μm) and mud (<63 μm) was analysed on all cores by wet sieving over 63 μm and subsequent dry sieving of the retained coarse fraction over 2 mm. Given the limited sample volume of ~48 cm^3, the gravel percentages determined for gravel-rich samples have to be considered as semi-quantitative contents (e.g., Head 2006). The grain-size data shown for the JR298 cores (Figs. 2–8) include gravel and sand contents only; the rest of the sediments consists of mud, i.e. silt and clay. Grain-size data presented for cores PS2556 and PS1565 (Figs. 9 and 10) also display the silt-clay ratios within the mud fraction.

Siliceous and calcareous biogenic components were removed from the mud fractions of cores PC727 and PC734 using 2M sodium carbonate and 1M dilute acetic acid, respectively, before their detailed grain-size distribution was measured with a Coulter Counter Multisizer-3 (MS3), to determine the mean grain size of terrigenous particles in the sortable silt fraction 10–63 μm ($\overline{SS}$) as a proxy for bottom-current speed (e.g., McCave and Hall 2006). The $\overline{SS}$ signal in marine sediments from polar regions can be affected by deposition of ice-rafted debris (IRD) (e.g., Hass 2002; McCave and Andrews 2019). In order to evaluate the IRD influence on $\overline{SS}$ of cores PC727 and PC734, percentage of sortable silt (SS%) in the fine fraction <63 μm was determined on selected samples by conducting a "one shot" pipette analysis at 10 μm threshold on the wet-sieved fine fraction. The mineralogical composition of the clay fraction (<2 μm) of cores PC727 and PC734 was investigated by X-ray diffraction (XRD) following Ehrmann et al. (2011).

Geochemical analyses of discrete samples included measurements of total carbon (TC) and total inorganic carbon (TIC) to determine $CaCO_3$ and total organic carbon (TOC) contents. TIC content was measured by acidifying the samples with an AutoMateFX carbonate preparation system and measuring evolved CO_2 with a UIC Coulometrics TM5011 CO_2 coulometer, and TC content was measured via combustion in a Flash Element Analyser (EA). TC and TOC were analysed on all samples from cores PC727, PC728 and PC734 and samples from selected intervals in cores PC723, PC726, PC732 and PC736. XRF measurements of major and trace element concentrations were conducted on discrete samples from cores PC723 and PC727 using an XRF spectrometer. The purpose of these analyses was to establish whether particular elemental ratios commonly used as palaeoproxies in marine sediments, such as the productivity proxies barium/aluminium (Ba/Al) and bromine/aluminium (Br/Al) (e.g., Bonn et al., 1998; Ziegler et al., 2008), showed identical down-core trends in the XRF data from discrete samples and scanning.

Stable oxygen ($\delta^{18}O$) and carbon ($\delta^{13}C$) isotope ratios using the VPDB standard on tests of the planktic foraminifera *Neogloboquadrina pachyderma* sinistral picked from the coarse fraction (>63 μm) of all samples containing sufficient tests in cores PC727, PC728, PC734 and PC736 and selected intervals in cores PC723 and PC727 were analysed with a Thermo-Finnigan MAT 253 mass spectrometer (2–26 tests per sample were picked, 10–12 tests were analysed on most samples). Age models for these cores were established by correlating their $\delta^{18}O$ data with the Marine Isotope Stages (MIS) of the LR04 benthic foraminifera $\delta^{18}O$ stack (Lisiecki and Raymo 2005). Marine Tephra B, a widespread tephra layer, which originates from a Plinian eruption of the Mt. Berlin volcano in Marie Byrd Land, West Antarctica, identified in Antarctic marine sediment and ice cores, was used as a marker for the MIS 5/MIS 6 boundary at ~130 ka (Hillenbrand et al., 2008a). Recently, an age of 130.7 ± 1.8 ka has been assigned to Marine Tephra B based on its identification in the Dome Fuji ice core in East Antarctica (Turney et al., 2020), which is, within error, consistent with age estimates from previously RPI-dated sediment cores from Drift 7 (Macrì et al., 2006; Hillenbrand et al., 2008a; Venuti et al., 2011).

Seabed surface sediments of GBC729 and GBC735 contained enough planktic foraminifera and other calcareous fossils to apply

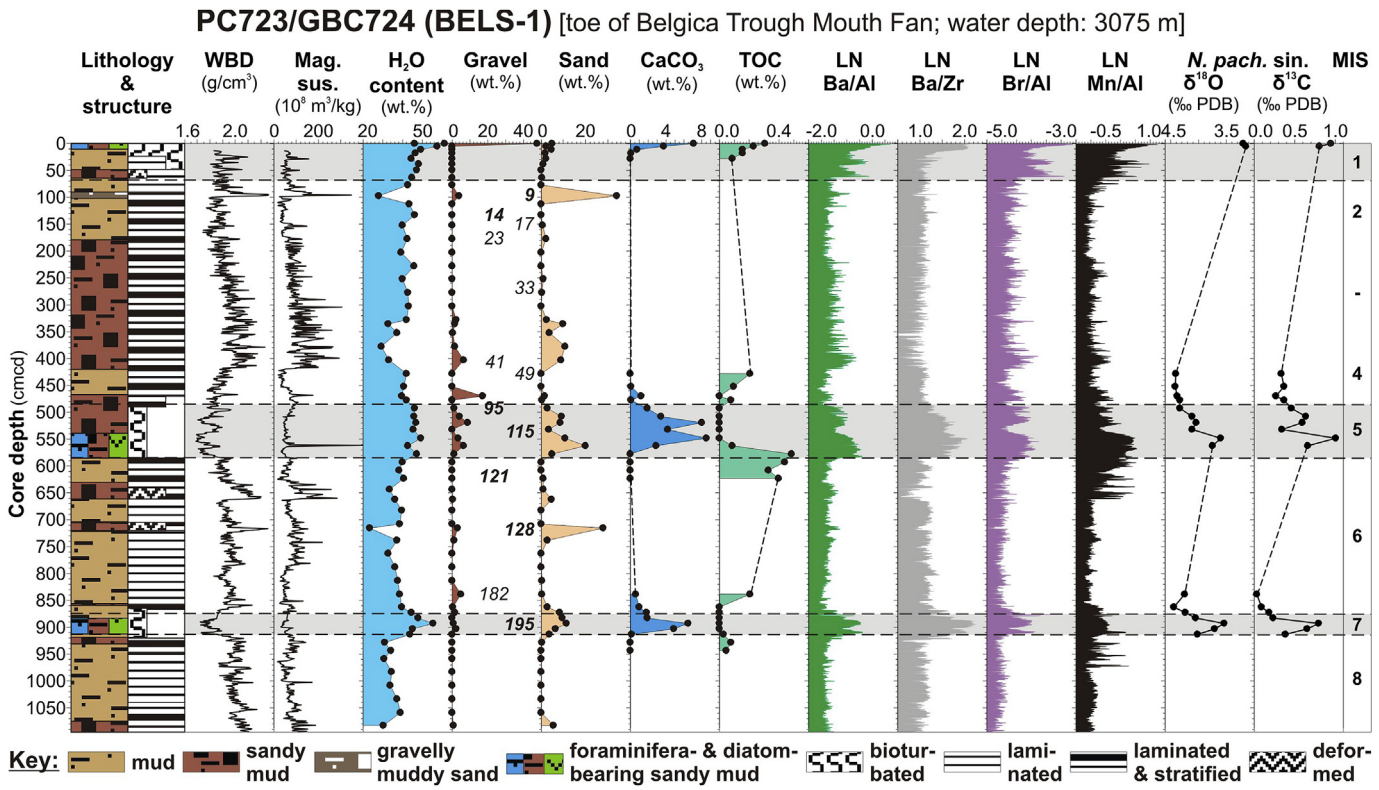

Fig. 2. Lithology, sedimentary structure (width of symbol reflects degree of bioturbation, lamination/stratification and deformation, respectively) and sedimentological data for core PC723/GBC724. Assignment of core intervals to Marine Isotope Stages (MIS) from Lisiecki and Raymo (2005) is also shown, with interglacial MIS highlighted by grey shading. Numbers in gravel column mark age-depth tie points (ages in ka) according to the RPI-based "trial" age model of Channell et al. (2019), which the authors consider to be of poor quality, with bold numbers highlighting interglacial ages.

AMS ^{14}C dating (Table 2). Four samples from GBC729 and two samples from GB735 were dated at Beta Analytic Inc., Miami, U.S.A., for testing the hypothesis that the frequent occurrence of manganese-coated gravel grains and cobbles at the surfaces of the JR298 GBCs resulted from current winnowing/non deposition.

All data presented for GCs PS1565-2 and PS2556-2 (incl. MUC PS2556-1) were analysed following the methods of Hillenbrand et al. (2003, 2005). Percentages of microfossils, micro-manganese (micro-Mn) nodules and volcanic glass particles shown for these cores were determined by identifying and counting 200–400 grains of the sand fraction (>63 μm) under a microscope (Hillenbrand 1994; Braun 1997). For the GCs grain-size samples were decalcified before analysis, and IRD abundance was determined on X-radiographs by counting gravel-sized clasts (>2 mm) continuously down-core at 1 cm depth intervals (Grobe 1987). Therefore, these two data sets are not directly comparable with those from the JR298 cores.

3. Results

Down-core data for all records (except GBC733) are shown in Figs. 2–13 and (except PS1565-2) are plotted versus centimetres composite depth (cmcd). The splicing of the PCs with the GBCs was conducted by visual correlation of (i) distinct lithological and structural features, and (ii) characteristic down-core changes and/or prominent peaks in physical properties, XRF scanner data, water content, TOC and $CaCO_3$ contents, and grain-size composition. The following splicing depths were determined: PC723, 20 cm = GBC724, 28 cm; PC726, 20 cm = GBC725, 32 cm; PC727, 20 cm = GBC730, 17 cm; PC728, 10 cm = GBC729, 7 cm; PC732, 17 cm = GBC731, 17 cm; PC734, 10 cm = GBC735, 15 cm; PC736, 9 cm = GBC722, 15 cm; GC PS2556-2, 0 cm = MUC PS2556-1, 13 cm. The splicing indicates ≤13 cm surface sediment loss in the long cores and, for GBC729 and GBC730, some sediment compression during sub-core retrieval. In the following, only the JR298 PC numbers and site numbers PS1565 and PS2556 are used for the spliced records, if not stated otherwise.

Only a box core was collected at site GBC733 from the channel between Drifts 5 and 5A. It recovered ~21 cm of bioturbated, diatom-bearing to diatomaceous mud overlying ~7 cm of laminated coarse silt and fine sand (Fig. S1). Because the succession was moderately disturbed, no detailed data are presented here.

3.1. Lithology and sedimentary structures

The recovered sedimentary sequences consist predominantly of terrigenous mud and sandy mud, with low and variable contents of sand and gravel (Figs. 2–10). Most of the sediments are laminated (layer thickness <1 cm) to stratified (layer thickness >1 cm), characterized by up to several centimetres thick, structureless muddy layers alternating with silty to sandy layers that are usually structureless, but occasionally laminated or stratified themselves. Very rarely, the coarse layers are normally graded and/or have an erosional base. Sediment intervals containing diatoms and/or foraminifera (nearly exclusively the planktic foraminifer *N. pachyderma* sin.) occur in all cores, and always bear dispersed gravel grains. These microfossil-bearing intervals are usually bioturbated to structureless, with their thicknesses ranging from ~10 cm to ~180 cm in the JR298 cores. All cores retrieved such a sediment type at their top, where also arenaceous benthic foraminifera were observed, with another biogenic interval occurring further down-core at sites PC726, PC727, PC734 and PS1565, and

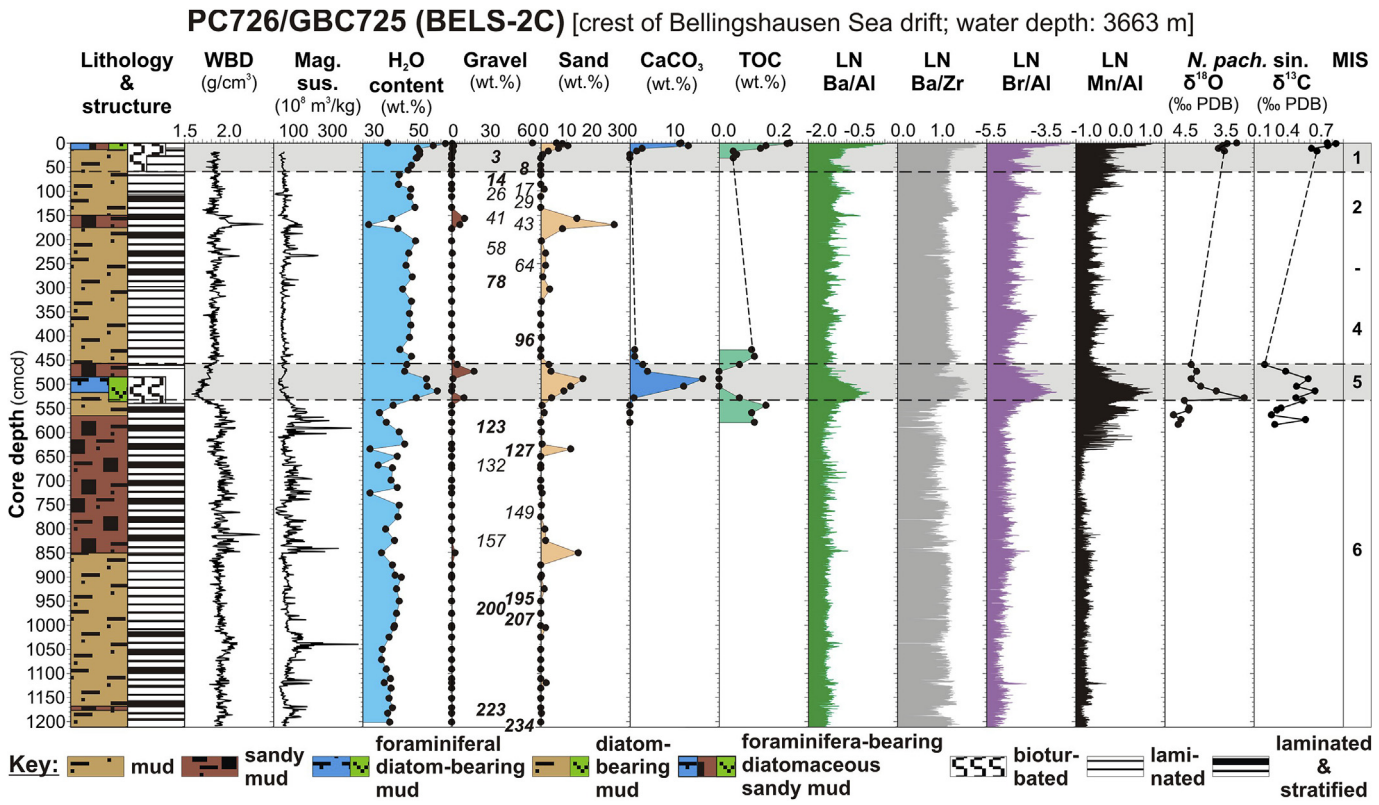

Fig. 3. Lithology, sedimentary structure (width of symbol reflects degree of bioturbation and lamination/stratification, respectively) and sedimentological data for core PC726/GBC725. Assignment of core intervals to Marine Isotope Stages (MIS) from Lisiecki and Raymo (2005) is also shown, with interglacial MIS highlighted by grey shading. Numbers in gravel column mark age-depth tie points (ages in ka) according to the RPI-based age model of Channell et al. (2019), with bold numbers highlighting interglacial ages.

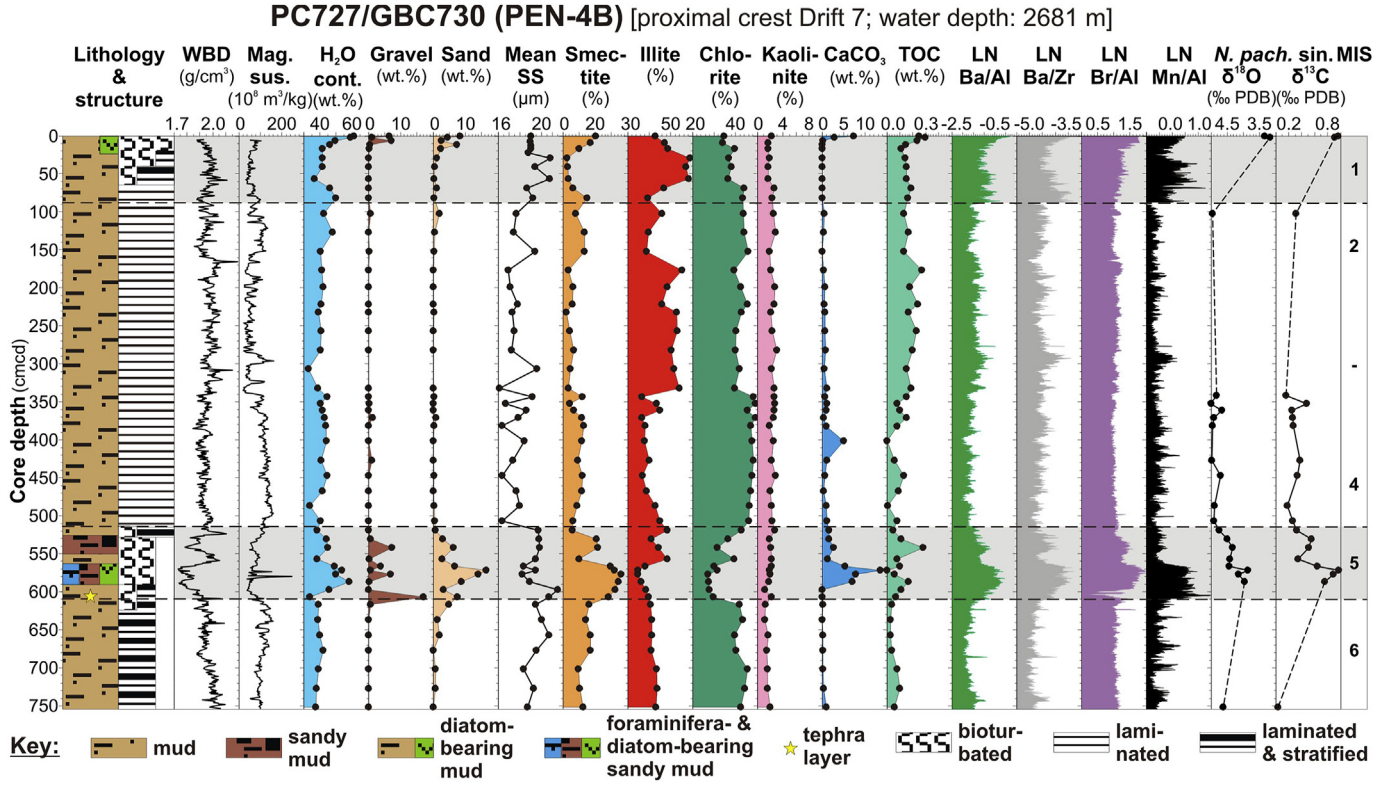

Fig. 4. Lithology, sedimentary structure (width of symbol reflects degree of bioturbation and lamination/stratification, respectively) and sedimentological data for core PC727/GBC730. Assignment of core intervals to Marine Isotope Stages (MIS) from Lisiecki and Raymo (2005) is also shown, with interglacial MIS highlighted by grey shading.

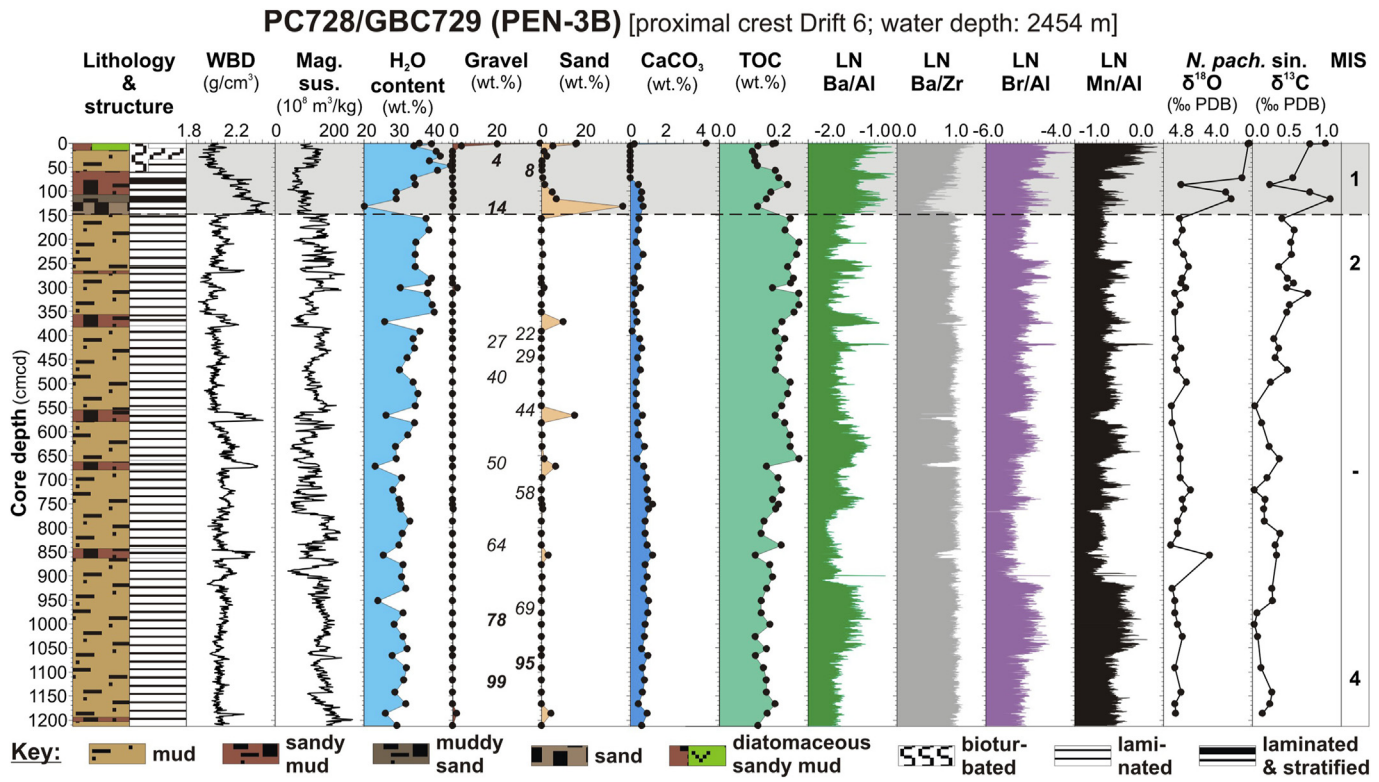

Fig. 5. Lithology, sedimentary structure (width of symbol reflects degree of bioturbation and lamination/stratification, respectively) and sedimentological data for core PC728/GBC729. Assignment of core intervals to Marine Isotope Stages (MIS) from Lisiecki and Raymo (2005) is also shown, with interglacial MIS highlighted by grey shading. Numbers in gravel column mark age-depth tie points (ages in ka) according to the RPI-based age model of Channell et al. (2019), with bold numbers highlighting interglacial ages.

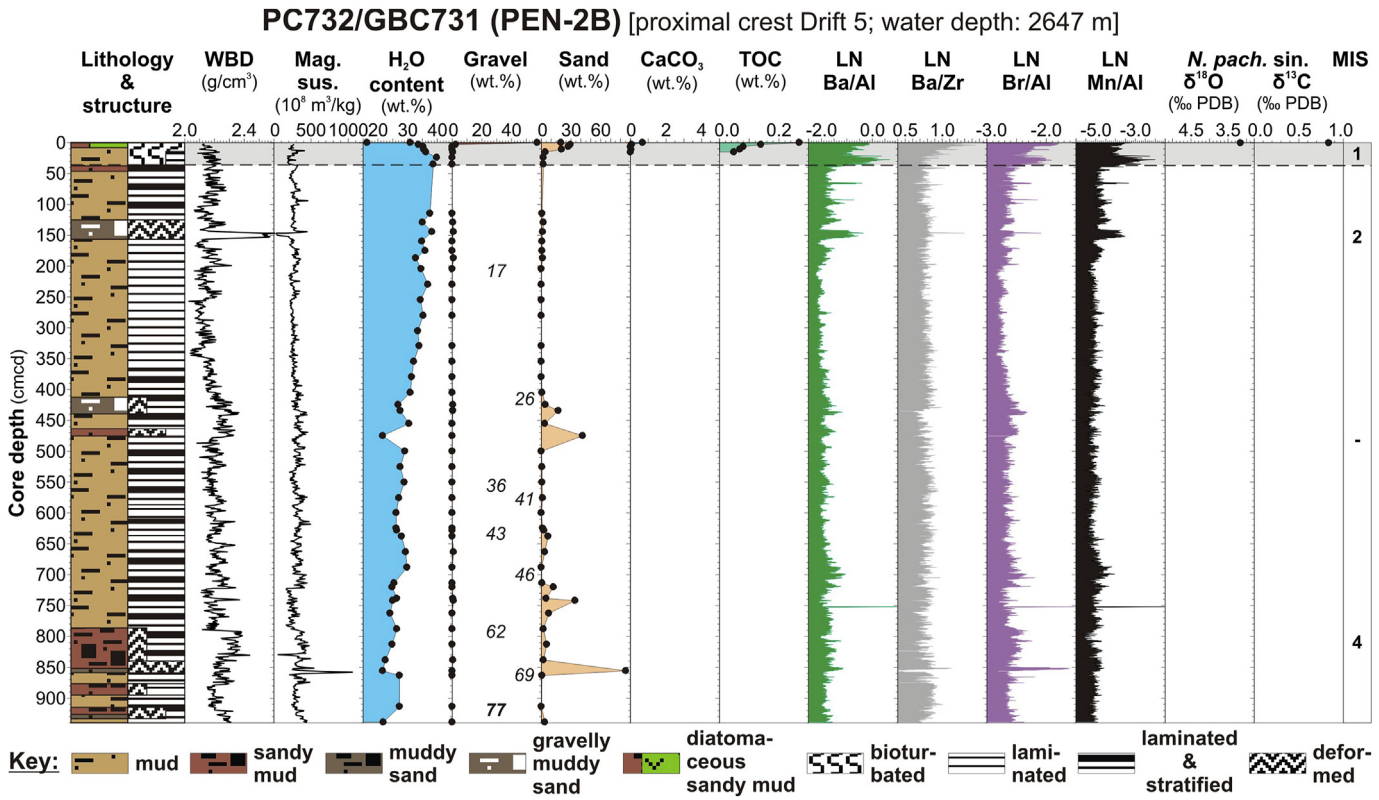

Fig. 6. Lithology, sedimentary structure (width of symbol reflects degree of bioturbation, lamination/stratification and deformation, respectively) and sedimentological data for core PC732/GBC731. Assignment of core intervals to Marine Isotope Stages (MIS) from Lisiecki and Raymo (2005) is also shown, with interglacial MIS highlighted by grey shading. Numbers in gravel column mark age-depth tie points (ages in ka) according to the RPI-based age model of Channell et al. (2019), with bold numbers highlighting interglacial ages.

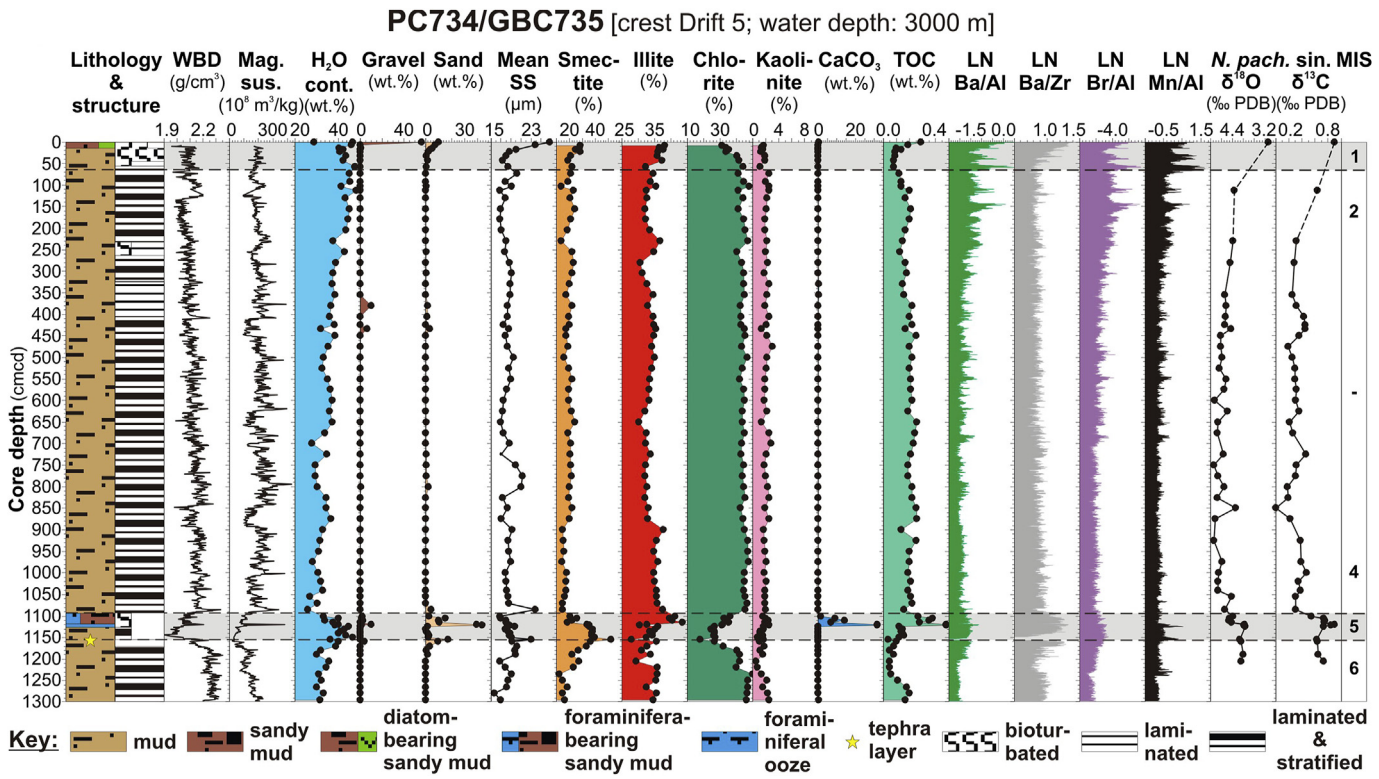

Fig. 7. Lithology, sedimentary structure (width of symbol reflects degree of bioturbation and lamination/stratification, respectively) and sedimentological data for core PC734/GBC735. Assignment of core intervals to Marine Isotope Stages (MIS) from Lisiecki and Raymo (2005) is also shown, with interglacial MIS highlighted by grey shading.

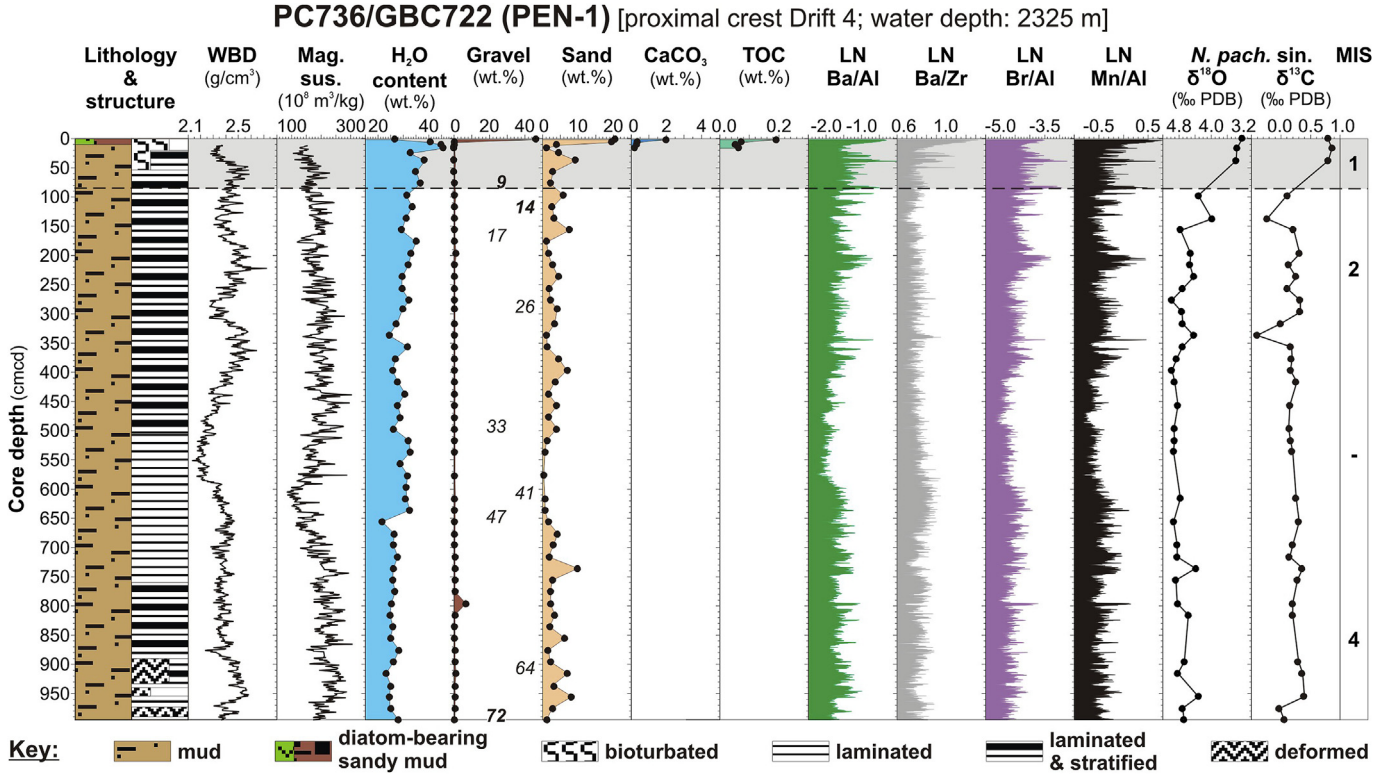

Fig. 8. Lithology, sedimentary structure (width of symbol reflects degree of bioturbation, lamination/stratification and deformation, respectively) and sedimentological data for core PC736/GBC722. Assignment of core intervals to Marine Isotope Stages (MIS) from Lisiecki and Raymo (2005) is also shown, with interglacial MIS highlighted by grey shading. Numbers in gravel column mark age-depth tie points (ages in ka) according to the RPI-based age model of Channell et al. (2019), with bold numbers highlighting interglacial ages.

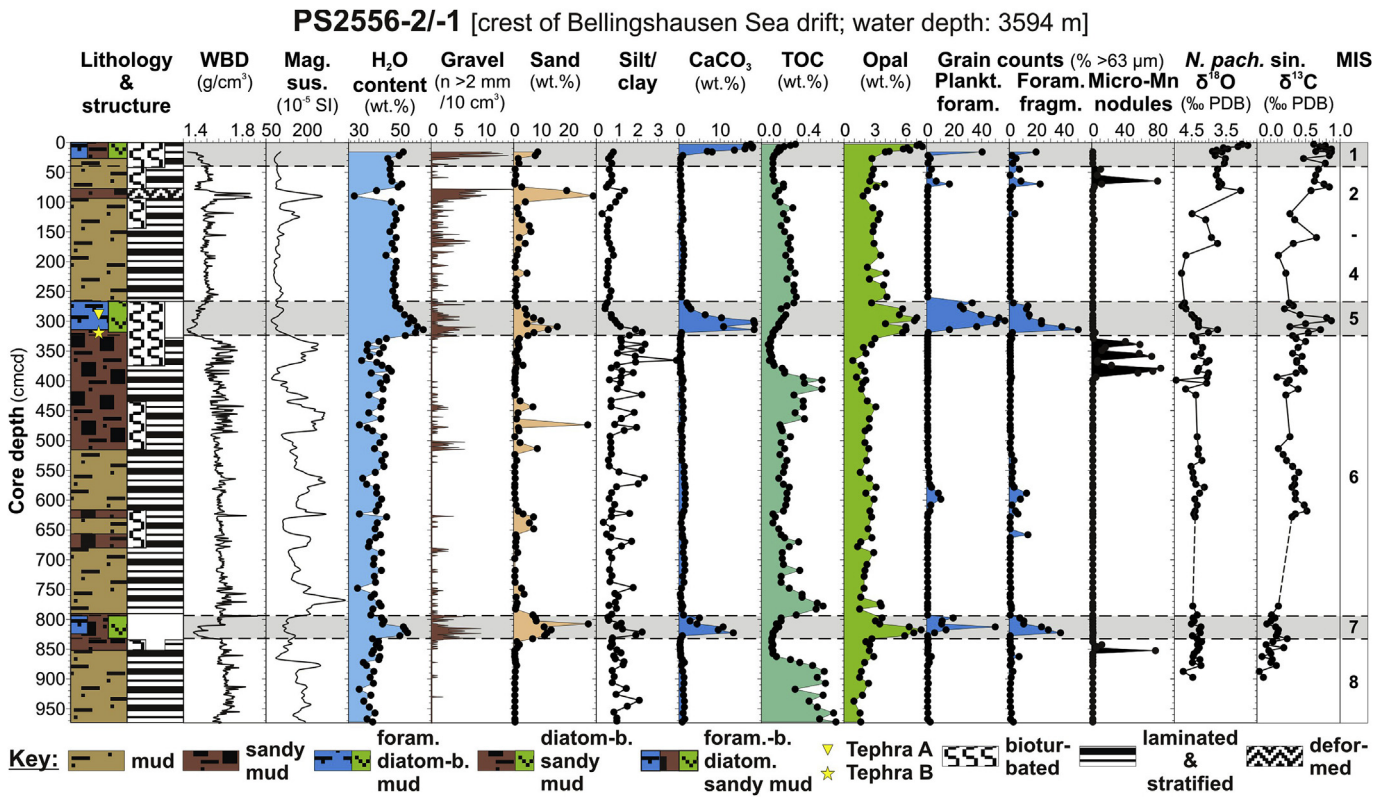

Fig. 9. Lithology, sedimentary structure (width of symbol reflects degree of bioturbation, lamination/stratification and deformation, respectively) and sedimentological data for core PS2556-2/-1. Assignment of core intervals to Marine Isotope Stages (MIS) from Lisiecki and Raymo (2005) is also shown, with interglacial MIS highlighted by grey shading.

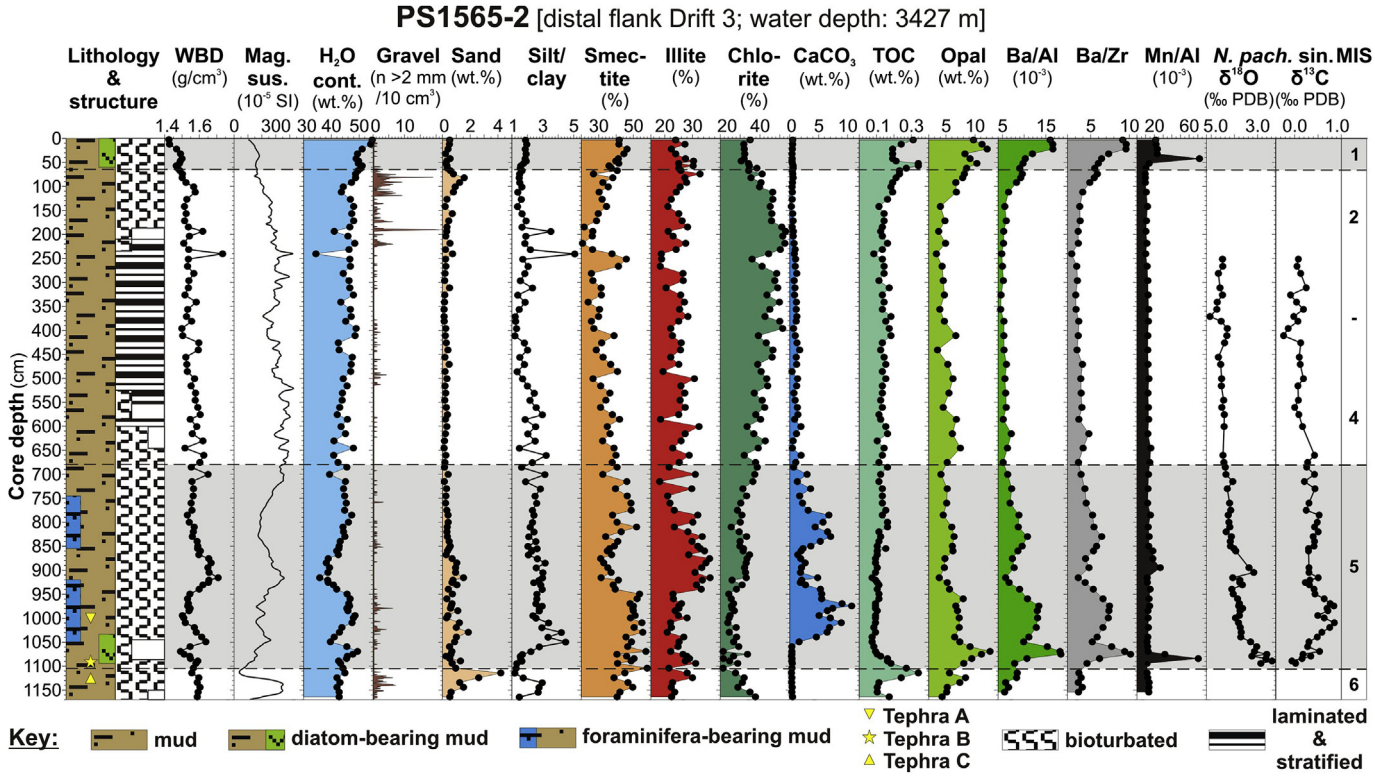

Fig. 10. Lithology, sedimentary structure (width of symbol reflects degree of bioturbation and lamination/stratification, respectively) and sedimentological data for core PS1565-2. Assignment of core intervals to Marine Isotope Stages (MIS) from Lisiecki and Raymo (2005) is also shown, with interglacial MIS highlighted by grey shading.

Table 2
Uncorrected AMS^{14}C dates on calcareous (micro-)fossils from seafloor surface sediments at sites GBC729/PC728 and GBC735/PC734.

Core ID	Sample depth	Laboratory code	Dated material	AMS^{14}C age (^{14}C yrs. BP)
GBC729/PC728	surface	Beta-407309	shell fragment bivalve	1360 ± 30
GBC729/PC728	surface	Beta-407310	shell fragment bryozoan	1370 ± 30
GBC729/PC728	surface	Beta-407311	shell fragment scaphopod	1360 ± 30
GBC729/PC728	surface	Beta-451924	planktic foraminifera	1260 ± 30
GBC735/PC734	surface	Beta-407312	shell fragment bivalve	1100 ± 30
GBC735/PC734	surface	Beta-451925	planktic foraminifera	1000 ± 30

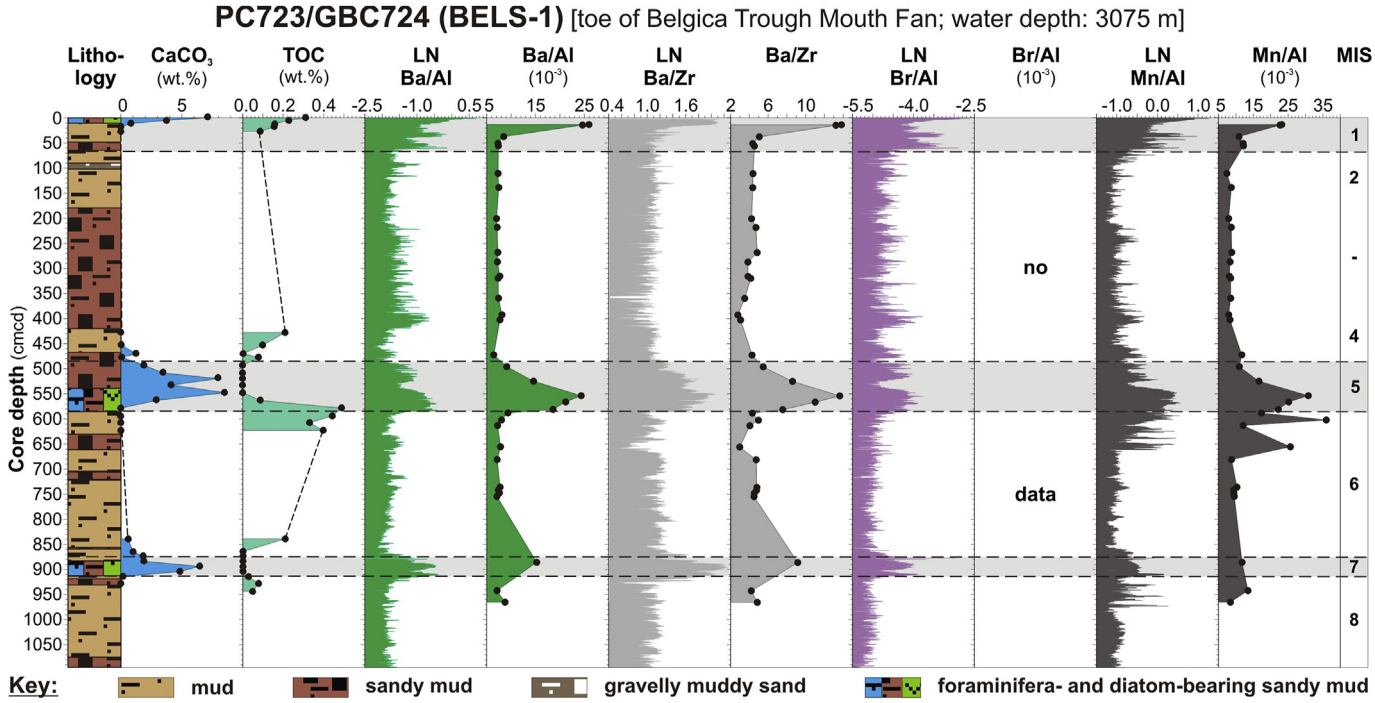

Fig. 11. Productivity proxies analysed on discrete samples (black dots) and with an XRF scanner in core PC723/GBC724. Mn/Al ratios are also shown.

two such intervals occurring down-core at sites PC723 and PS2556 (Figs. 2–4, 7, 9, 10).

Subordinate sedimentary structures include cross lamination, observed only once in a thin interval of core PC734 (305–310 cmcd), and deformation structures, mainly at site PC732. The deformation structures comprise bending, sloping, faulting and fanning of coarse- and fine-grained layers as well as convolute bedding. One horizon at site PC732 contained a slab of semi-consolidated sand that is orientated obliquely to the core axis. The structures are embedded between horizontally laminated and stratified intervals and are therefore considered to be primary features rather than coring or splitting artefacts.

A tephra layer sitting stratigraphically just below the second microfossil-bearing interval from the surface was found in cores PC727 and PC734 (Figs. 4 and 7). In core PC734 the tephra formed a ~4 cm thick, slightly bioturbated macroscopic bed (1153–1157 cmcd), whereas it was recognizable as a microscopic or "disseminated" tephra layer in core PC727. Tephra layers undetectable by visual logging, but identified by microscopic investigations of smear slides or extracted coarse grained fractions are nowadays referred to as "cryptotephra" (e.g. Davies 2015). Notwithstanding the recent claim by Di Roberto et al. (2019), such microscopic/dispersed tephra layers originating from distinct individual volcanic eruptions have been identified in Antarctic marine sediment cores since at least the 1970s (e.g., Huang et al., 1975; Kyle and Seward 1984; Shane and Froggatt 1992), with both micro- and macroscopic tephra layers having been reported from the western Antarctic Peninsula margin and the Bellingshausen Sea, including cores PS2556 and PS1565 (Figs. 9 and 10; Hillenbrand et al., 2008a and references therein). Sand fraction samples were taken from cores PC723 and PC726 from similar stratigraphic positions to the occurrence of the tephra layers in cores PC727 and PC734, but glass shards were detected in core PC726 (530–535 cmcd) only, where they were present in low concentrations (<5%).

3.2. Physical properties and grain size

Pronounced down-core changes in magnetic susceptibility, WBD and water content reflect predominantly the major lithological changes, i.e. the alternations between bioturbated/structureless biogenic sediments and laminated/stratified terrigenous sediments. Thereby, magnetic susceptibility and WBD display minima and water content displays maxima in the biogenic intervals (Figs. 2–10). Furthermore, discrete magnetic susceptibility and WBD peaks correlate with individual large (mafic) gravel grains or, in the terrigenous intervals, discrete coarse-grained layers.

Overall, sand and gravel concentrations are low in the cores, but they are consistently elevated in the biogenic intervals. Notably, the seafloor surface sediments at all JR298 sites except PC727 display absolute maxima in gravel concentrations, associated with elevated

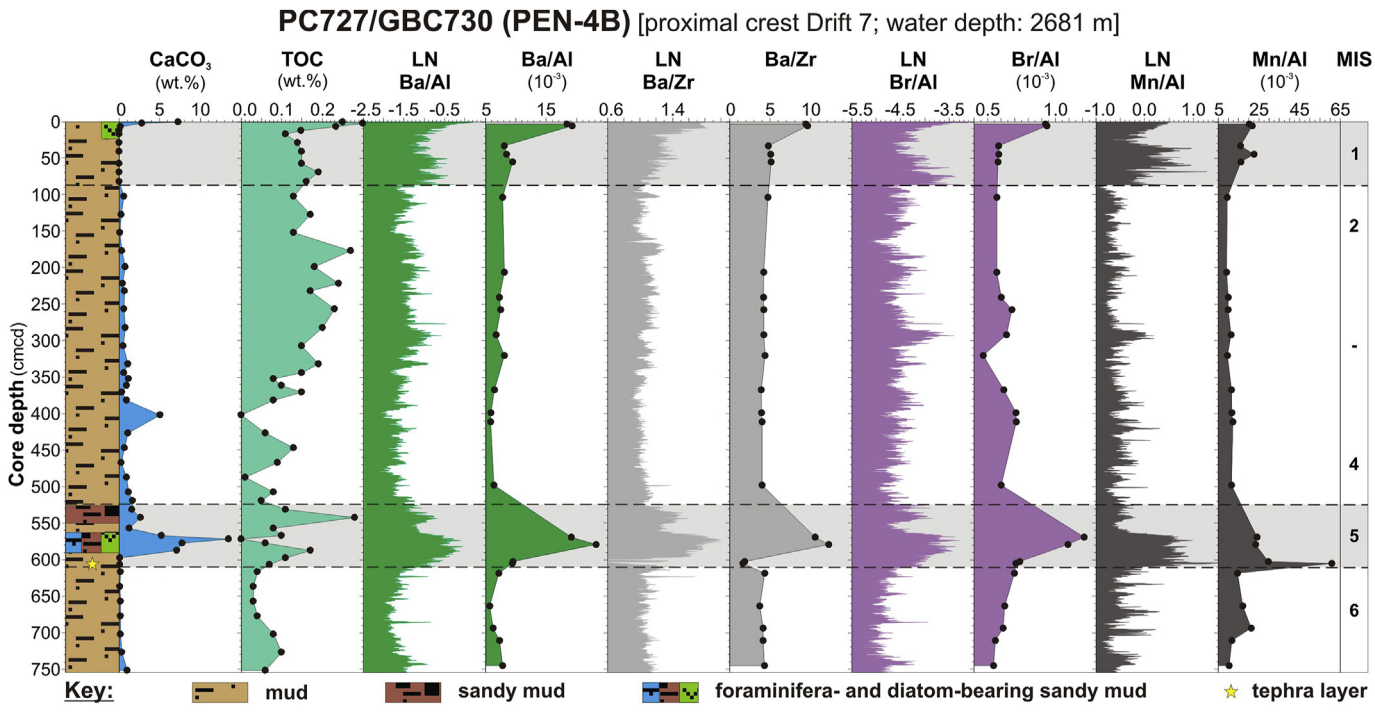

Fig. 12. Productivity proxies analysed on discrete samples (black dots) and with an XRF scanner in core PC727/GBC730. Mn/Al ratios are also shown.

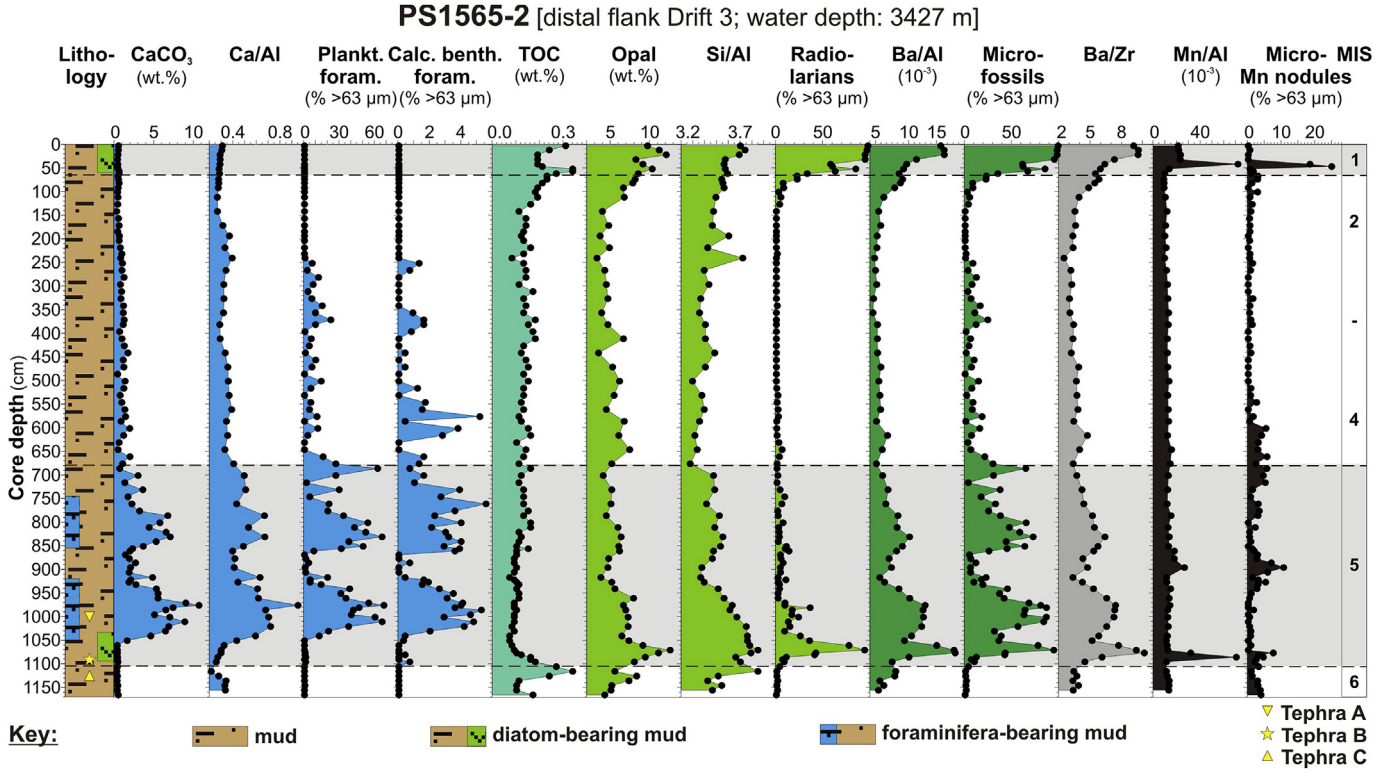

Fig. 13. Productivity proxies analysed on discrete samples (black dots) in core PS1565-2. Mn/Al ratios and abundances of micro-Mn nodules (in the fraction >63 µm) are also shown.

sand contents. Even at site PC727, the core-top gravel and sand contents are considerably increased. This finding is corroborated by photographs of the GBC surfaces showing dispersed, often manganese-coated gravel grains and cobbles (Fig. 14; Fig. S1).

$\overline{SS}$ in core PC727 varies from 19 to 22 µm within both the biogenic intervals and the terrigenous interval directly underlying the deeper biogenic interval. In the other terrigenous interval $\overline{SS}$ predominantly ranges from 16 to 19 µm (Fig. 4). In contrast, $\overline{SS}$ in core PC734 varies mainly between 16 and 21 µm, without showing a clear difference between biogenic and terrigenous intervals

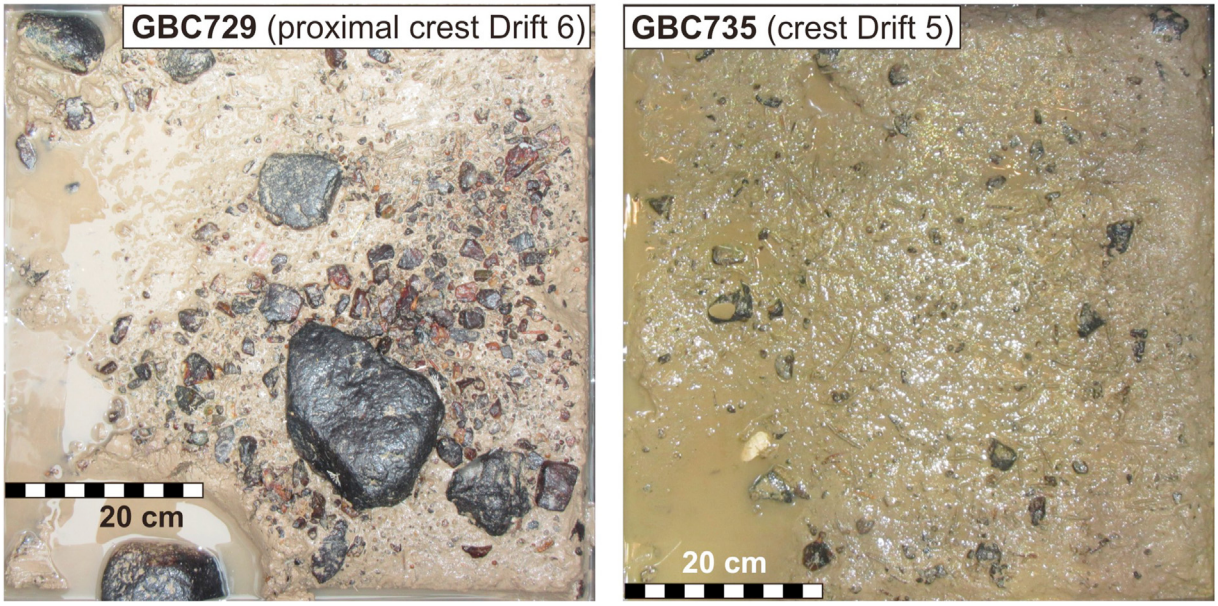

Fig. 14. Seafloor surface sediments recovered at sites GBC729/PC728 and GBC735/PC734. AMS^{14}C dates obtained from calcareous (micro-)fossils from the two samples are given in Table 2.

(Fig. 7). However, similar to the gravel content, $\overline{SS}$ reaches an absolute maximum in the (near-)surface sediments at site PC734 (>22 μm). Furthermore, the tephra layer in core PC734 is characterized by relative sand and $\overline{SS}$ maxima (Fig. 7).

SS% and $\overline{SS}$ show a positive correlation for cores PC727 and PC734 (Fig. S2), with a significant correlation for PC727 (coefficient R = 0.74; just a single data point is responsible for reducing R from 0.93 to 0.74). The data for PC734 show more scatter (R = 0.53), probably because of the presence of unsorted iceberg-delivered silt and clay (e.g., McCave and Hall 2006). According to McCave and Andrews (2019), a running down-core correlation coefficient R_{run} of >0.5 is required for interpreting the $\overline{SS}$ of IRD-influenced sediments as a record of bottom-current speed.

3.3. Geochemical parameters and clay mineral composition

$CaCO_3$ concentrations reach their maxima at the seafloor surfaces of most sites (Figs. 2–13). Exceptions are PC734 from 3000 m and PS1565 from 3427 m water depth, which are the deepest sites west of the Antarctic Peninsula. At present, the water depth of the Calcite Compensation Depth (CCD) seems to drop westwards from ~2800 m water depth on the Antarctic Peninsula margin to ~3000 m in the Bellingshausen Sea (Hillenbrand et al., 2003). In many of the cores the $CaCO_3$ concentrations decrease to nearly zero immediately below the surface maximum, but in cores PC728 and PS1565 they remain slightly and continuously elevated (≥0.5 wt%) in the underlying terrigenous interval, thereby showing a minor down-core increase (Figs. 5 and 10). In the sub-surface biogenic intervals of cores PC723, PC726, PC727, PC734 and PS2556 the $CaCO_3$ concentrations are considerably higher (Figs. 2–4, 7, 9). Similar $CaCO_3$ down-core patterns were previously reported from core PS1565 (Fig. 10; Hillenbrand and Fütterer 2002) and other sediment cores west of the Antarctic Peninsula (Pudsey and Camerlenghi 1998; Pudsey 2000).

Similarly to the $CaCO_3$ content, TOC content decreases immediately down-core beneath a maximum concentration at the seafloor surface at most sites. However, TOC remains elevated in the underlying terrigenous intervals of cores PC727, PC728, PC734 and PS2556 (Figs. 4, 5, 7 and 9). In core PC734 the $CaCO_3$ maximum at ~1120 cmcd coincides with a TOC maximum (Fig. 7). This contrasts with cores PC723, PC726, PC727 and PS2556, in which these down-core $CaCO_3$ maxima coincide with TOC minima (Figs. 2–4, 9, 11).

Biogenic barium (Ba_{bio}) is considered the most reliable palaeoproductivity proxy in Late Quaternary sediments recovered south of the Antarctic Polar Front (e.g., Bonn et al., 1998; Hillenbrand and Cortese 2006; Jaccard et al., 2013). Consequently, barium counts measured with an XRF scanner and normalised for terrigenous input using titanium or aluminium (e.g., Presti et al., 2011) are widely used as a proxy for Ba_{bio} in these sediments. Ba/Al ratios for the investigated cores are higher in the biogenic intervals but their maxima often lie stratigraphically below $CaCO_3$ maxima, especially near the seabed surface (Figs. 2–8, 10-13). Because high Ba contents in sediments can also result from an increased supply of detrital barite rather than increased biological productivity, we also normalised Ba with respect to zirconium (Zr), which is a proxy for zircon and thus detrital heavy minerals.

Bromine has also been proposed as a proxy for marine organic carbon content in sediment cores (e.g., Ziegler et al., 2008), including most cores studied here (Channell et al., 2019). In general, the down-core trends of the Br/Al data reflect those of the Ba/Al data in all XRF-scanned cores (Figs. 2–8). Furthermore, the Br/Al ratios of discrete samples from core PC727 match the Br/Al data obtained from XRF scanning (Fig. 12), indicating that the Br/Al down-core variations are unlikely to reflect changes in water content only, which can influence XRF scanner data for elements dissolved in high concentrations in seawater and/or pore-water (Tjallingii et al., 2007; Ziegler et al., 2008; Hennekam and De Lange 2012).

Normalised manganese (Mn) ratios in marine sediments are commonly used as a proxy for Mn-oxide concentration, an indicator of the oxygenation state of the bottom water at the time of deposition (e.g., Jaccard et al., 2016; Wagner and Hendy 2017; Wu et al., 2018). In most of our investigated cores, Mn/Al ratios exhibit maxima in the biogenic intervals (Figs. 2–8, 10), which is also consistent with the Mn-coating of gravel and cobbles at the seabed surface (Fig. 14; Fig. S1). In general, the Mn/Al ratios match

the down-core Ba/Al and Br/Al patterns, but, notably, they also show maxima in the terrigenous sediments directly underlying the biogenic intervals (Figs. 2–8), which is particularly evident from the abundance of micro-Mn nodules in core PS2556 (Fig. 9). Mn/Al ratios analysed on discrete samples from cores PC723 and PC727 confirm this observation (Figs. 11 and 12). In core PS1565 maxima in Mn/Al ratios of bulk sediments coincide with maximum abundances of micro-Mn nodules (Figs. 10 and 13).

As in core PS1565 (Fig. 10; Hillenbrand and Ehrmann 2002), clay mineral assemblages in cores PC727 and PC734 consist mainly of chlorite, illite and smectite, with only very minor contents of kaolinite (Figs. 4 and 7). In the three cores, smectite tends to be higher in the biogenic intervals, whereas chlorite shows higher concentrations in the terrigenous sediments (Figs. 4, 7, 10 and 15). Along the core transect, smectite generally decreases at the expense of chlorite and illite in a SW-ward direction (Fig. 15).

3.4. Chronological constraints

The planktic $\delta^{18}O$ data exhibit low ratios in the biogenic sediments and high ratios in the terrigenous intervals, with the $\delta^{13}C$ data often showing an opposite pattern (Figs. 2–10). Where resolved, the $\delta^{18}O$ shift at the transition between the biogenic interval at the core top and the underlying terrigenous sediments is ~1.5‰ (Figs. 4, 5, 7–9), corresponding to the typical global $\delta^{18}O$ shift of 1.0–1.5‰ caused by the combined effect of decreasing ice volume and ocean warming at Late Quaternary glacial terminations, which is recorded by benthic and planktic foraminifera (e.g. Imbrie et al., 1984; Lisiecki and Raymo 2005; Elderfield et al., 2012). The corresponding planktic $\delta^{13}C$ changes in our cores are on average 0.6‰, ranging from 0.3‰ (PC734) to 0.7‰ (PC727, PC728), and thus also lie within the range of typical global glacial-interglacial $\delta^{13}C$ shifts recorded by benthic foraminifera, although the entire whole-ocean change probably did not exceed 0.3 ± 0.2‰ (e.g. Peterson et al., 2014; Gebbie et al., 2015). In the biogenic intervals of the middle and lower parts of our cores, the $\delta^{18}O$ decreases with respect to under- and overlying terrigenous sediments vary from 0.5‰ to 1.7‰, but, with an average range of 0.9‰, are generally less prominent than near the core top. The corresponding $\delta^{13}C$ increases, with an average range of 0.5‰, are only slightly less prominent (Figs. 2–4, 7, 9).

AMS ^{14}C dates were obtained from calcareous epi-faunal organisms and planktic foraminifera (*N. pachyderma* sin.) from the seafloor surface sediments of GBC729 (=PC728) and GBC735 (=PC734) (Fig. 14). For site GBC735, a bivalve shell and planktic foraminifera provided uncorrected ages of 1100 and 1000 ^{14}C yrs BP, respectively, while for site GBC729 benthic organisms and planktic foraminifera gave slightly older ages of ~1360 and 1260 ^{14}C yrs BP, respectively (Table 2). Thus, the ages from site GBC729 match the pre-bomb marine reservoir effect (MRE) of ~1300 ^{14}C yrs BP in the Southern Ocean, whilst those from site GBC735 lie within the pre-bomb MRE and the post-bomb MRE of ~700 ^{14}C yrs BP (e.g. Berkman and Forman 1996; Berkman et al., 1998; Skinner et al., 2019). The planktic foraminifera ages are slightly younger than those from the calcareous benthos at both sites, reflecting the slightly lower MRE in Southern Ocean surface waters when compared to bottom waters (e.g., Sikes et al., 2000). In general, however, the ^{14}C dates document a recent age of biogenic particles at the core tops. No down-core AMS ^{14}C ages are available.

The stratigraphic positions of the tephra layers in cores PC727 and PC734 (Figs. 2 and 7) and sand-sized glass shards found in core PC726 (530–535 cmcd) match that of Marine Tephra B in numerous cores from the study area (Hillenbrand et al., 2008a), including cores PS2556 and PS1565 (Figs. 9 and 10). Tephra B has an age of 130.7 ± 1.8 ka (Turney et al., 2020). Marine Tephra A, detected in both cores PS2556 and PS1565, was assigned an age of ~92 ka, whilst Marine Tephra C in core PS1565 has a likely age of ~136 ka (Hillenbrand et al., 2008a).

In view of these chronological results, together with the observed down-core fluctuations in palaeoproductivity proxies, especially the Ba/Al ratios which are usually unaffected by dissolution, the biogenic intervals at the core surfaces are assigned to interglacial MIS 1, the first sub-surface biogenic intervals in cores PC723, PC726, PC727, PC734, PS1565 and PS2556 to interglacial MIS 5, and the deeper biogenic intervals in cores PC723 and PS2556 to interglacial MIS 7. Consequently, the terrigenous intervals in between are assigned to the glacial periods MIS 2–4, 6 and 8. We acknowledge that there is some uncertainty, as to whether the first sub-surface biogenic interval spans the entire MIS 5 or MIS 5e only, and the same question arises for the second biogenic interval regarding MIS 7 and MIS 7e, respectively. In cores PC723, PC726, PC727, PC734 and PS1565 the planktic $\delta^{18}O$ data of the first sub-surface biogenic interval reach their interglacial peak values (corresponding to MIS 5e) near the base of this interval, coinciding with maximum Ba/Al ratios (Figs. 2–4, 7, 10). The upper part of the interval, which is characterized by slightly lower Ba/Al ratios and maximum $CaCO_3$ contents, displays slightly higher but still relatively low $\delta^{18}O$ ratios. This suggests that the biogenic interval spans the entire MIS 5, which is also consistent with the constraints from Marine Tephras A and B for cores PS2556 and PS1565 (Figs. 9 and 10). In analogy, we assign the whole of MIS 7 to the second sub-surface biogenic interval. These assignments are consistent with

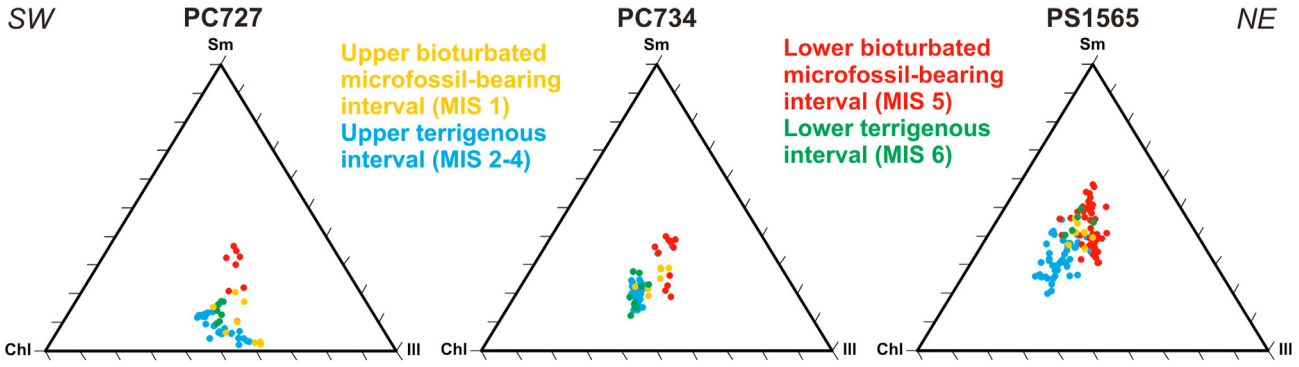

Fig. 15. Ternary diagrams for clay mineral assemblages across the core transect PS1565 – PC734 – PC727 from NE to SW along the Antarctic Peninsula continental rise (data for core PS1565 are from Hillenbrand and Ehrmann 2002). Clay mineral assemblages were recalculated on a kaolinite-free basis because kaolinite is present in trace amounts (≤3%) only. Clay mineral data from smectite-enriched tephra layers are excluded.

previous age assignments for cores from both the study area (Pudsey and Camerlenghi 1998; Pudsey 2000; Sagnotti et al., 2001; Hillenbrand and Ehrmann 2002; Lucchi et al., 2002; Villa et al., 2003; Macrì et al., 2006; Venuti et al., 2011; Vautravers et al., 2013) and the East Antarctic continental margin (Grobe and Mackensen 1992; Bonn et al., 1998; Wu et al., 2017; Jimenez-Espejo et al., 2020).

We provide the age-depth tie points for our cores, including linear sedimentation rates, in Table 3. Importantly, these age models are predominantly based on a combination of δ^{18}O-, tephro- and lithostratigraphy, whereas in previous studies only the age model for core PC466 from Drift 4, which was recovered in close proximity to site PC736, had some chronological constraints from planktic δ^{18}O data (Vautravers et al., 2013). Our new age models document that sedimentation rates during glacial periods were consistently higher than during the preceding or subsequent interglacial periods (Table 3; Fig. S3). Our age assignments are generally consistent with the RPI-based age models for some of the JR298 cores published in Channell et al. (2019) (Fig. S3a–d), and we discuss the discrepancies in section 4.4.

4. Interpretation and discussion

4.1. Sediment facies and depositional processes

We distinguish four major **Facies A** to **D** and three subordinate and rarely occurring **Facies E** to **G** (Table 4; Fig. 16; Supplementary Text). These facies strongly resemble sediment types previously reported from the western Antarctic Peninsula rise by Pudsey and Camerlenghi (1998), Pudsey (2000), Lucchi et al. (2002) and Lucchi and Rebesco (2007) but have to be considered as "end-members" because especially the laminated to stratified facies vary and transition down-core over a few decimetres or even several centimetres. **Facies A** is bioturbated to structureless, occurs at all sites and consists of (sandy) mud bearing biogenic material and dispersed gravel grains interpreted as IRD (Fig. 16a,b). These hemipelagic sediments are assigned to MIS 1, 5 and 7 (Figs. 2–13). The boundary between **Facies A** and the other facies is often transitional, with bioturbation of laminated to stratified sediments suggesting that any primary sedimentary structures within **Facies A** (e.g., layers formed by bottom-current activity) were subsequently obliterated by burrowing infauna.

Facies B, C, D, E and **F** usually lack biogenic components and bioturbation, probably as a consequence of perennial sea-ice coverage during glacial periods, and are assigned to glacial MIS 2–4, 6 and 8 (Figs. 2–13). As shown by Lucchi and Rebesco (2007) for a network of cores recovered from Drift 7 and Pudsey (2000) for cores recovered from the crests of the other drifts, these sediment types result from the interplay of contouritic, turbiditic, meltwater plume and IRD deposition, with the dominant process varying both with the location of a core on the rise (i.e., on a drift or near a channel, on the crest or flank of a drift, proximal or distal to the adjacent shelf) and the time of deposition (i.e., at the beginning, during the peak or at the end of a glacial period, during MIS 2–4 or MIS 6). Laminated to stratified **Facies B** consists of mud alternating with well defined silty-sandy layers and often, but not always, contains rare gravelly IRD (Fig. 16c). In the cores from the drifts its sediments are probably mainly contourites derived from detritus originally transported down the continental slope by debris flows and slumps that were initiated by the advance of grounded ice masses across the shelf during glacial periods. At the base of the slope, the material went into suspension forming turbidity currents. Fine-grained particles in the upper parts of the suspension clouds were entrained into a benthic nepheloid layer, which covered the rise in the areas surrounding the channels, and captured by the SW-ward flowing bottom current before being deposited on the drifts together with IRD that had been released by passing icebergs (Pudsey and Camerlenghi 1998; Lucchi et al., 2002; Lucchi and Rebesco 2007). Thus, the grain-size changes reflected by the lamination and stratification of **Facies B** are likely to result from both variability in bottom-current speed and turbiditic supply of silt and sand to the nepheloid layer. At the shelf proximal drift crest sites PC727, PC728, PC732 and PC736, **Facies B** probably includes plumite material delivered by meltwater plumes emanating from the grounding line of the APIS, when it was located at the nearby shelf break during glacial periods (e.g., Pudsey and Camerlenghi 1998; Pudsey 2000; Lucchi and Rebesco 2007). At deep sites PC723 from the toe of Belgica TMF and PS1565, located close to a channel on the distal western flank of Drift 3, **Facies B** intervals without IRD may include thin, distal turbidites (cf. Lucchi et al., 2002). **Facies B** includes the cross-laminated mud and silt observed in a single interval of core PC734 (Fig. 16d). Because of the drift crest location of site PC734, enhanced bottom current speed rather than turbidity current flow seems to be the most likely mechanism for the formation of this cross lamination, which is supported by evidence for strong bottom-current vigour in neighbouring core PC107 (Pudsey 2000).

Facies C comprises mud that is faintly laminated due to the

Table 3
Age-depth tie points and linear sedimentation rates (LSR) for the investigated sediment cores. Ages for Marine Isotope Stage (MIS) boundaries are from Lisiecki and Raymo (2005). The LSR given for the lowermost part of a core is an estimated minimum based on the assumption that the next older interglacial sediments at the site lie just below the maximum penetration depth of the core.

MIS	Age (ka)	PC723/GBC724	PC726/GBC725	PC727/GBC730	PC728/GBC729	PC732/GBC731	PC734/GBC735	PC736/GBC722	PS2556	PS1565
		Depth (cmcd)	Depth (cmcd)	Depth (cmcd)	Depth (cmcd)	Depth (cmcd)	Depth (cmcd)	Depth (cmcd)	Depth (cmcd)	Depth (cm)
1	0	0	0	0	0	0	0	0	0	0
1/2	14	68	60	89	149	34	55	85	40	65
4/5	71	485	459	512	≥1217	≥940	1092	≥996	267	679
5/6	130	585	533	610			1155		323	1105
6/7	191	824	≥1212	≥757			≥1295		793	≥1171
7/8	243	912							832	
8/9	300	≥1095							≥975	
MIS	**Age (ka)**	**LSR (cm/kyr)**	**LSR (cm/kyr)**	**LSR (cm/kyr)**	**LSR (cm/kyr)**	**LSR (cm/kyr)**	**LSR (cm/kyr)**	**LSR (cm/kyr)**	**LSR (cm/kyr)**	**LSR (cm/kyr)**
1	0–14	4.86	4.29	6.36	10.64	2.43	3.93	6.07	2.85	4.64
2–4	14–71	7.32	7.00	7.42	≥17.14	≥13.24	18.19	≥15.98	3.98	10.77
5	71–130	1.69	1.25	1.66			1.07		0.95	7.22
6	130–191	3.92	≥11.13	≥2.41			≥2.30		7.70	≥1.08
7	191–243	1.69							0.75	
8	243–300	≥3.20							≥2.51	

Table 4
Facies identified in the JR298 sediment cores.

Facies	Lithology	Sediment composition	Sedimentary structures	Clay mineral assemblage	Climatic setting	Interpretation	Cores
A	mud with dispersed gravel grains	biogenic-bearing	bioturbated to structureless	high smectite	interglacial	hemipelagite with IRD	All GBCs and PCs
B	mud alternating with thin silt and sandy silt layers; occasionally with normal gradation	terrigenous	laminated to stratified; cross laminated	high chlorite	glacial	contourite; meltwater plumite (at drift crest sites); distal turbidite (at distal flank and deep sites)	PC723/GBC724, PC726/GBC725, PC727, PC728, PC732, PC734, PC736
C	mud alternating with faint, slightly coarser layers or subtle, (sub-) millimetre thin silt laminae	terrigenous	faintly laminated to faintly stratified	high chlorite	glacial	contourite; meltwater plumite	PC723, PC726, PC727/ GBC730, PC728, PC732, PC734, PC736
D	mud alternating with gravelly sand and sandy gravel layers or with dispersed sand and gravel grains	terrigenous	laminated to stratified	high chlorite	glacial	contourite with winnowed layers (lag deposits); hemipelagite alternating with IRD layers; meltwater plumite (at proximal crest sites)	PC723, PC726/GBC725, PC727/GBC730, PC728, PC732, PC734, PC736
E	very coarse silt to sand; +/− erosional base; +/− normal gradation	terrigenous	structureless to laminated to stratified	high chlorite	glacial	proximal turbidite; current reworked deposit	PC726, PC728, GBC733
F	mud with silty and sandy layers; occasionally with gravel grains	terrigenous	deformed; laminated to stratified	high chlorite	glacial	slump deposit; debris-flow deposit	PC723, PC732, PC734, PC736
G	bed of silty to sandy volcanic glass	terrigenous	slightly bioturbated	high smectite	T-II	airfall tephra	PC734

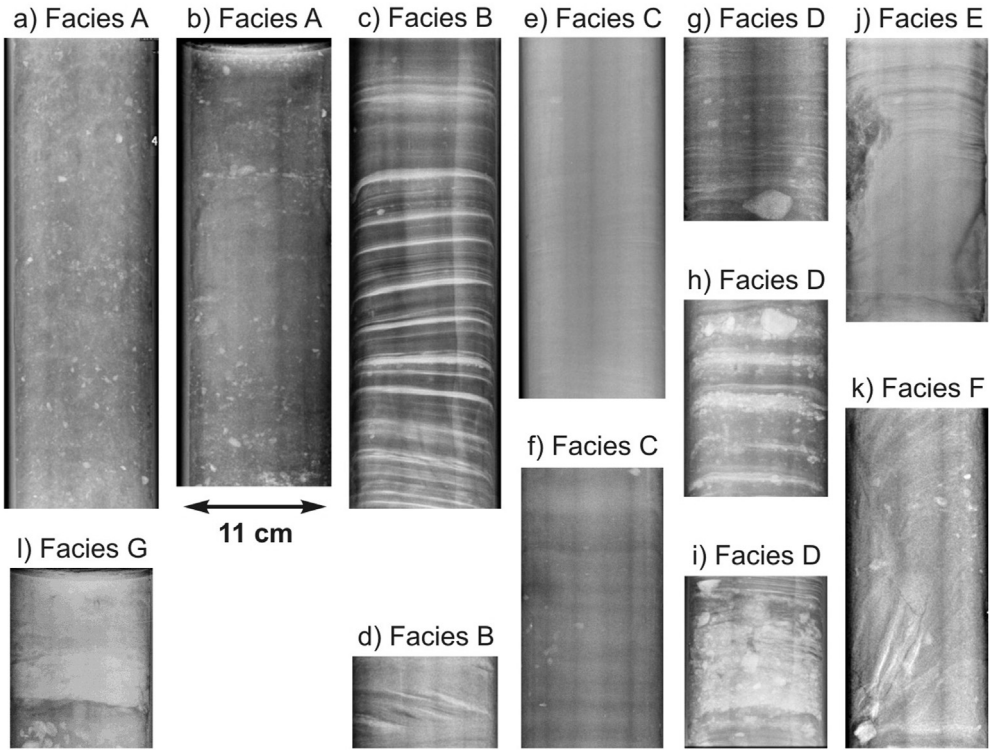

Fig. 16. Example X-radiographs (negatives) for facies identified in the JR298 cores (Table 4). **a) Facies A**: bioturbated mud with dispersed gravel grains; **b) Facies A**: structureless mud with dispersed gravel grains; **c) Facies B**: mud alternating with thin silt and (partly normally graded) sandy silt layers; **d) Facies B**: cross-laminated mud alternating with silt; **e) Facies C**: faintly laminated mud with subtle (sub-)millimetre thin silt laminae; **f) Facies C**: faintly stratified mud; **g) Facies D**: laminated mud with dispersed gravel grains; **h) Facies D** mud alternating with gravelly sand and sandy gravel layers; **i) Facies D**: mud with a bed of normally graded sandy gravel to gravelly sand; **j) Facies E**: normally graded sand overlain by laminated to stratified muddy sand; **k) Facies F**: deformed mud with silty to sandy layers and dispersed gravel grains; **l) Facies G**: slightly bioturbated bed of silty to sandy volcanic glass.

presence of very thin, delicate silt laminae or faintly stratified due to very subtle grain-size changes (Fig. 16e and f). It contains no or only rare sand and gravel grains that are either dispersed or form isolated, very widely spaced thin layers. This facies is most prominent in proximal drift crest cores PC727 and PC728 and usually alternates with **Facies B** and **D**. The sediments of **Facies C** resemble those observed in cores from the crest of Drift 7 that were interpreted as fine-grained contourites with a variable meltwater plume component (Lucchi et al., 2002; Lucchi and Rebesco 2007). **Facies D** comprises terrigenous mud either alternating with a few

millimetre thin to several centimetre thick sandy-gravelly layers or bearing abundant dispersed sand and gravel grains (Fig. 16g–i). These sediments are interpreted as (i) contourites, with the coarse-grained layers being lag deposits resulting from current winnowing (cf. Ó Cofaigh et al., 2001), (ii) hemipelagic deposits, with the gravel grains and coarse layers resulting from episodically high IRD input (cf. Pudsey and Camerlenghi 1998), and (iii), predominantly in the shelf proximal drift crest cores, meltwater plumites that still contained sand close to their source (cf. Lucchi and Rebesco 2007).

Very rare **Facies E** occurs in cores PC727, PC728 and GBC733 (from the channel separating Drifts 5 and 5A) only and consists of structureless and laminated to stratified very coarse silt and sand. Its sediments, which can have an erosional base, are interpreted as gravitational downslope deposits. **Facies E** in core PC728 (97–148 cmcd) comprises structureless sand fining upward into sandy mud overlain by stratified and laminated sandy mud (Fig. 16j) and is interpreted here as a proximal turbidite with a bottom-current reworked top. **Facies F** cannot easily be distinguished from coring disturbance as it is characterized by deformed mud with silty-sandy layers and dispersed gravelly IRD (Fig. 16k). These sediments occur frequently at site PC732 on Drift 5, where likely fluid escape structures were observed (Suppl. Text; Fig. S4), and are interpreted as slump and debris-flow deposits. **Facies G**, which comprises a slightly bioturbated bed of silty-sandy volcanic glass particles, was only observed at site PC734 (Fig. 16l). Based on its stratigraphic position (Fig. 7), the tephra bed was identified as Marine Tephra B (section 3.4.).

4.2. Comparison of proxies for productivity

The most complete sets of palaeoproductivity data come from cores PC723, PC727 and PS1565 (Figs. 11–13). Biogenic barium is a reliable palaeoproductivity proxy under oxygenated conditions (e.g. Bonn et al., 1998; Hillenbrand and Cortese 2006; Jaccard et al., 2013). Oxic conditions at our core sites towards the end of glacials and during interglacials are evident from high Mn/Al ratios and the occurrences of micro-Mn nodules (Figs. 2–13) as well as the presence of Mn-coated dropstones at the seafloor surfaces (Fig. 14; Fig. S1). Lucchi and Rebesco (2007) concluded from the absence of biogenic components and bioturbation in glacial-age drift sediments (corresponding to our **Facies B** to **F**) and the presence of the mineral pyrrhotite in these sediments (Sagnotti et al., 2001) that oxygen-depleted bottom waters had bathed the Antarctic Peninsula continental rise during Late Quaternary glacial periods. However, a subsequent comprehensive study of the magnetic mineralogy of these sediments by Venuti et al. (2011) documented an absence of pyrrhotite, and negligible/trace amounts of iron (Fe) sulphides. Recently, Channell et al. (2019) concluded for the JR298 cores that the authigenic mineral maghemite is present throughout the sediment column recovered by the PCs. Maghemite is formed at (and near) the seafloor surface by oxidation of (detrital) magnetite. In pelagic sediments maghemite is dissolved at the oxic-anoxic boundary, typically just a few decimetres below the surface. In the drift sediments, however, sub-surface dissolution of maghemite is significantly reduced, thereby varying between sites, and maghemite is present down to at least ~10 m below the seafloor (Channell et al., 2019). This strongly suggests that our Ba_{bio} records do not result from variable down-core dissolution (Figs. 2–8, 10).

We consider the possibility that the interglacial Ba/Al maxima in our cores could have resulted from a higher supply of terrigenous barite. Like zircon, this detrital heavy mineral is typically enriched in the sand fraction, which is increased in the interglacial intervals (Figs. 2–10), reflecting the higher IRD content that characterises **Facies A** (section 4.1., Suppl. Text; Figs. 14 and 16; Fig. S1). The Ba/Zr data match the Ba/Al data in all XRF scanned cores, indicating that the Ba/Al maxima result from a high Ba_{bio} supply during interglacial periods (Figs. 2–8). The Ba/Al and Ba/Zr data available from discrete samples of cores PC723, PC727 and PS1565 corroborate these findings (Figs. 10–13).

The Br/Al data measured with the XRF scanner (Figs. 2–8) reveal a very good correlation with those measured on discrete samples (core PC727; Fig. 12), with maxima observed during interglacials. Br has been used as a palaeoproductivity proxy in marine sediments, for example by Ziegler et al. (2008), who demonstrated that high Br contents in sediments reflect higher marine organic carbon content rather than terrestrial organic material. This assertion is supported by the fact that the Br/Al data in the JR298 cores mirror the Ba/Al data (Figs. 2–8, 12).

Apart from a positive correlation in the near-surface sediments, we observe no clear relationship between TOC and Br/Al or TOC and Ba/Al, but at sites PC723, PC726, PC727, PC734 and PS1565 maxima in Ba/Al and/or Br/Al during MIS 5 and 7 coincide with very low TOC contents (Figs. 2–4, 7, 10-13). This suggests that organic matter below the seafloor surface, and especially in glacial sediments (cf. PC728, Fig. 5), predominantly consists of old refractory carbon, whilst degradable, non-refractory carbon has been dissolved. In support of this, a close inspection of the sand fraction from Termination II sediments in core PS1565, which are characterized by a prominent TOC maximum preceding the MIS 5 maximum in Ba/Al ratios and other productivity proxies (Fig. 13), revealed the presence of a coal fragment. The coal was probably supplied as IRD, which is suggested by a sand maximum coinciding with the TOC maximum at Termination II (Fig. 10). A similar TOC peak is also observed at Termination I in core PS1565. In addition, in core PC101 from Drift 1, the record with continuous down-core TOC data nearest to site PS1565 (Fig. 1), TOC maxima at both Termination I and Termination II also precede interglacial Ba/Al maxima (Pudsey, unpublished). This hints at a significant source for fossil organic matter on the part of the Antarctic Peninsula margin adjacent to Drifts 1, 2 and 3.

The interglacial Ba/Al maxima coincide with maxima in biogenic opal, siliceous microfossils and Si/Al ratios (Figs. 10 and 13; note: a minor opal maximum preceding Termination II in core PS1565 is caused by the presence of Marine Tephra C, Hillenbrand et al., 2008a). The opal maxima are caused by maxima in diatom abundance and also radiolarian abundance (Fig. 13; cf. Pudsey and Camerlenghi 1998; Pudsey 2000; Villa et al., 2003). The $CaCO_3$ maxima during interglacials originate predominantly from maxima in the abundances of planktic foraminifera, with only minor contributions from calcareous benthic foraminifera (Figs. 9 and 13). In addition, rare occurrences of calcareous nannofossils have been reported from the intervals with the highest $CaCO_3$ contents (Villa et al., 2003).

In all of our cores spanning past interglacials, the Ba/Al maxima and (where measured) the opal maxima lead the $CaCO_3$ maxima, which is most evident in the cores with expanded MIS 5 intervals (Figs. 2–4, 7, 9-13). This distinctive sequence of maxima in various palaeoproductivity proxies was previously reported from records recovered below ~2000 m water depth on the East Antarctic margin between 15° W and 44° E (Grobe and Mackensen 1992; Bonn et al., 1998), our study area (Pudsey and Camerlenghi 1998; Pudsey 2000; Hillenbrand and Fütterer 2002; Villa et al., 2003) and the continental margin offshore from Prydz Bay (Wu et al., 2017). It has been attributed to a maximum in primary productivity, evident from the Ba/Al maximum, during peak interglacial conditions, which resulted in a maximum flux of fresh degradable, organic carbon to the seafloor. The subsequent remineralisation of this organic material resulted in a shallowing of the CCD, so that only siliceous microfossils were preserved (Grobe and Mackensen 1992; Bonn et al., 1998; Hillenbrand and Fütterer 2002). A decrease in productivity

during the later, cooler part of an interglacial, and perhaps even during the early part of a glacial, caused a deepening of the CCD that led to the preservation of calcareous microfossils and, thus, dilution of siliceous microfossils in the sediments. Accordingly, $CaCO_3$ maxima coincide with moderate Ba/Al ratios (e.g., Figs. 10 and 13). A CCD deepening throughout interglacials is also reflected by productivity proxies in core PS2556: increases in opal content during early MIS 7 and early MIS 5 are initially followed by maxima in calcareous foraminifera fragments, and these peaks are in turn followed by maxima in whole foraminiferal test concentrations (Fig. 9).

4.3. Diagenetic manganese enrichments and their implications for the geochemical record

A new finding in our study from the West Antarctic margin are distinct Mn-enrichments at the end of glacials and during interglacials. These enrichments are evident from high Mn/Al ratios and high abundances of sand-sized micro-Mn nodules within the cores (Figs. 2–13) and Mn-coated dropstones at the seafloor surface (Fig. 14; Fig. S1). In cores PC723, PC726 and PC727, high Mn/Al ratios during MIS 5 and MIS 7 coincide with high Ba/Al ratios and $CaCO_3$ maxima that are also characterized by a complete absence of TOC (Figs. 2–4). In addition, some subordinate Mn/Al spikes occur in late MIS 6 and late MIS 8 (and, to a lesser extent, late MIS 2) sediments in these cores. At sites PC734, PS1565 and especially PS2556, high Mn/Al ratios and maxima in micro-Mn nodules, respectively, coincide with TOC minima that precede productivity peaks during MIS 1, 5 and 7 (evident from maxima in Ba/Al and Br/Al ratios and/or opal contents).

In previous work, Pudsey and Camerlenghi (1998) reported micro-Mn nodules from MIS 6 sediments on Drift 7 and explained their occurrence with condensed deposition, whilst Pudsey (2000) described micro-Mn nodules associated with *Chondrites* burrows from MIS 1 sediments at sites PC107 (Drift 5), PC109, PC110 (both Drift 4A), PC111 (Drift 4) and PC113 (Drift 3). Furthermore, XRF data from discrete samples of core PC106 (Drift 6) presented by Pudsey (2000; see their Fig. 6b) showed a MnO-peak in sediments of late MIS 6 age. However, the Al-normalised Mn data of this core reveal two, more prominent and broad, maxima which bracket Marine Tephra B (Hillenbrand et al., 2008a) and comprise Termination I to MIS 1, respectively (Pudsey, unpublished). As in our cores with XRF data from discrete samples (Figs. 11–13), the Mn/Al ratios at sites PC106 and PC111 reached their highest ratios around glacial terminations (Pudsey, unpublished).

Manganese enrichments at the end of glacial periods and during interglacials were previously reported from other parts of the deep Southern Ocean, including the Antarctic continental margin (e.g., Mangini et al., 1990, 2001; Presti et al., 2011; Jaccard et al., 2016; Wagner and Hendy 2017; Wu et al., 2018; Jimenez-Espejo et al., 2020). Often these Mn-enrichments are explained by the presence of well-oxygenated Antarctic Bottom Water (AABW), whose production restarted or intensified at the end of glacial periods, when grounded ice began to retreat from the shelf and allowed the formation of AABW precursor water masses in sub-ice shelf cavities and shelf polynyas (Wu et al., 2018; Jimenez-Espejo et al., 2020). However, as in other ocean basins (e.g., Mangini et al., 1990; 2001; Kasten et al., 2004; Funk et al., 2004a, 2004b; Löwemark et al., 2014), it needs to be kept in mind that Mn in marine sediments is dissolved in pore-water under sub- and anoxic conditions and precipitated at the redoxcline, which forms the base of the oxic zone and usually is situated just a few decimetres (or even a few centimetres) below the seafloor surface. Under steady-state diagenetic conditions, the oxic-suboxic boundary, and thus also the horizon of solid-phase Mn-enrichment, will remain at a constant depth with respect to the sediment surface over time (Kasten et al., 2004). This implies that under continued sediment deposition Mn is constantly dissolved below and, after transport in pore-water towards the seafloor surface, precipitated at an upward migrating Mn-redox front (e.g., Kasten et al., 2004; Presti et al., 2011).

Relict redox fronts, such as those manifest in Mn-enrichments, can be preserved in down-core sediments when a front shifts rapidly upwards (e.g., Kasten et al., 2004), the depositional environment is characterized by low supply of labile organic carbon (De Lange et al., 1994), or the grain size of the Mn-precipitates (such as the micro-Mn nodules in PS1565 and PS2556) is larger than that of the host sediments (e.g., Mangini et al., 1990). Furthermore, the pore-water oxygen content at the depth of the relict front has to remain sufficiently high to prevent complete dissolution of the precipitated element oxide/hydroxide. In most instances, relict redox fronts indicate non-steady-state diagenetic conditions that could have been initiated by: (1) changes in organic carbon burial induced by variations in sedimentation rate, organic carbon supply to the seafloor and/or oxygen content of bottom water, (2) rapid sediment burial associated with deposition of turbidites, debris flows, slumps, etc., (3) variable upward diffusive flux of reduced components (such as methane) from deeper in the sediment column, and (4) changes in pore water/fluid flow from greater sediment depths or across the seawater-seabed interface (e.g., De Lange et al., 1994; Kasten et al., 2004). For the cyclic deposition of Mn-rich layers in the Arctic Ocean, a dramatically increased supply of dissolved Mn from the surrounding continental shelves via recycling from shelf sediments and landmasses derived from fluvial input has been identified as an additional, crucial factor (Löwemark et al. 2012, 2014). The processes summarised under (1) change particularly rapidly during the transition from a glacial to an interglacial period, so that relict redox fronts are frequently preserved across glacial terminations (e.g., Mangini et al., 2001; Funk et al., 2004a, 2004b; Kasten et al., 2004; Reitz et al., 2004; Jimenez-Espejo et al., 2020). However, the geochemical mobility of Mn in the sediments before a Mn-enriched layer is eventually "fixed" in the sedimentary record reduces the usefulness of such layers for core correlations, which is apparent from their sometimes variable stratigraphic position on an ocean-basin wide or even regional scale (e.g., Löwemark et al., 2014; Meinhardt et al., 2016; Jimenez-Espejo et al., 2020). This also should be taken into account when using Mn-enrichments in sediment cores for identifying and interpreting the exact timing of bottom water oxygenation during a glacial-interglacial cycle.

Well oxygenated bottom-water conditions at our core sites during the present interglacial MIS 1 are documented by the Mn-enrichments in the surface sediments (Figs. 2–13), and especially the Mn-coating of the dropstones on the seafloor (Fig. 14; Fig. S1). The bottom water bathing the drifts is derived from oxygen-rich deep-water masses originating in the Weddell Sea (Camerlenghi et al., 1997; Giorgetti et al., 2003; Hillenbrand et al., 2008b; Hernández-Molina et al., 2017). Mn-enrichments are also observed across Terminations I, II and III and during MIS 5 and MIS 7, but their exact stratigraphic positions slightly vary between the cores (Figs. 2–13). We consider that the onset of well oxygenated bottom-water conditions at our sites during glacial terminations, which may not necessarily be expressed in a change in bottom-current vigour (section 4.5.), caused a down-ward progression of the Mn-redox front (e.g., Kasten et al., 2004), thereby causing Mn-precipitation within sediments deposited at the end of glacial periods (Table 5).

The reliable palaeoproductivity proxies Ba/Al and Br/Al often document a sharp increase of biological productivity at the beginning of interglacials, with the productivity remaining high

Table 5
Reconstructed changes in the investigated sedimentary records throughout Late Quaternary glacial-interglacial cycles.

Climatic Conditions	General lithology	Sediment composition	Sedimentary structures	Clay mineralogy assemblage	Productivity proxies	Bottom-water O_2 oxygenation	Mn-redox front position
Moderate (late) interglacial	mud with dispersed IRD	biogenic-bearing; mainly planktic foraminifera; rare calcareous benthic foraminifera	bioturbated/ structure-less; decreasing upward pumping of IRD	smectite decreasing	elevated Ba/Al, Br/Al but decreasing; high $CaCO_3$; elevated/decreasing opal; increasing refractory TOC	elevated, but decreasing	stagnation
Peak interglacial	mud with dispersed IRD	biogenic-bearing; mainly diatoms, radiolarians; arenaceous foraminifera (MIS 1 only)	bioturbated/ structureless; upward pumping of IRD	high smectite	max. Ba/Al, Br/Al, opal; elevated/nil $CaCO_3$ (depending on water depth); low/nil non-refractory TOC (MIS 7, MIS 5), high non-refractory TOC (MIS 1)	high	initial rapid upward shift followed by stagnation
Glacial termination	mud with rare IRD	terrigenous	laminated/ stratified	chlorite decreasing	Ba/Al, Br/Al, opal low but increasing; nil $CaCO_3$; min. TOC (but high refractory TOC (in PS1565 due to iceberg rafting)	rapidly increasing	downward migration
Glacial	mud with rare IRD	terrigenous	laminated/ stratified	high chlorite	min. Ba/Al, Br/Al; low/nil opal; low/nil $CaCO_3$; elevated refractory TOC	initially decreasing then low (still oxic)	initial rapid upward shift followed by migration in pace with sedimentation

throughout peak interglacials. In case of MIS 1, this increase is also evident from the high TOC contents in the surface sediments (Figs. 2–13). The associated increased input and burial of degradable marine organic carbon should have shifted the redox fronts upwards toward the seafloor surface, but it has been shown that metastable element enrichments, such as the Mn-spikes in the late glacial sediments of our cores, can be preserved when this shift happens suddenly (De Lange et al., 1994; Kasten et al., 2004). Alternatively, no such upward shift might have happened because the increase in degradable carbon supply was insufficient to overcome the supply of well oxygenated bottom water (Table 5). The continued bathing of the drifts with this water mass during an interglacial would have caused very efficient remineralisation of the non-refractory, degradable organic matter at the seafloor and within the uppermost part of the seabed. This is evident from the TOC minima observed at the end of glacial MIS 6 and MIS 8, as well as during interglacial MIS 5 and MIS 7 in the cores spanning these time periods (Figs. 2–4, 7, 9-13). Most of our records with continuous down-core TOC data, especially PC728, PC734 and PS2556 (Figs. 5, 7 and 9), also indicate that this process affected organic matter across Termination I, but the corresponding TOC minima are often less pronounced, probably because the remineralisation of marine organic carbon is still ongoing.

Notably, TOC minima of (just above) 0 wt.% from late MIS 8 into MIS 7 and from late MIS 6 into MIS 5, respectively, are observed in the westernmost cores PC723, PC726, PC727 and PS2556 as well as in core PC734, which was collected further east but also from relatively deep water (3000 m). These TOC minima reveal considerable "burn-down" of organic carbon, i.e. post-depositional oxidation of non-refractory organic matter (Figs. 2–4, 7, 9), implying that (i) sedimentation rates during the corresponding times did not exceed 1–2 cm/kyr (Jung et al., 1997; Mangini et al., 2001; Kasten et al., 2004), and (ii) the input of fossil, refractory organic material was at a minimum. We argue that both the burn-down of organic carbon at a glacial termination and during the early part of an interglacial caused by the availability of well oxygenated bottom water and the decrease in the input of degradable, marine organic matter during the latter part of an interglacial, evident from the decreases in Ba/Al and Br/Al, resulted in the oxic-suboxic boundary remaining stationary at a similar level in the seabed over thousands to tens of thousands of years, even under continued sediment deposition, leading to the recorded Mn-enrichments (cf. Kasten et al., 2004) (Table 5). The apparently lower stratigraphic positions of the TOC minima and Mn-enrichments across Terminations II and III in core PS2556 when compared to cores PC723 and PC726, where the most prominent Mn-enrichments and coinciding TOC minima are observed in the MIS 5 and MIS 7 sediments, respectively, may hint at a deeper downward progression of the oxidation front or its longer persistence in the late glacial sediments at site PS2556 (Table 5), probably as a result of a lower sedimentation rate at this site (Figs. 2, 3 and 9; Table 3). We highlight the joint occurrence of TOC minima and peaks in micro-Mn nodule abundance at site PS2556. Sedimentation rates <1–2 cm/kyr, required for major burn-down of organic carbon, are also a prerequisite for growth of Mn-nodules (e.g., Löwemark et al., 2012; Dutkiewicz et al., 2019). The ages of 130 ka for Marine Tephra B and 92 ka for Marine Tephra A (Hillenbrand et al., 2008a) yield a linear sedimentation rate of 0.9 cm/kyr for the corresponding MIS 5 sediment interval at site PS2556 (Fig. 9). Such low sedimentation rates, which may have persisted across glacial terminations at site PS2556, are consistent with organic carbon burn-down and Mn-nodule growth.

We assume that during glacial periods, when the bottom waters bathing the Antarctic margin and the deep Southern Ocean became less ventilated in response to drastically reduced AABW production (e.g., Jaccard et al., 2016; Wu et al., 2018; Jimenez-Espejo et al., 2020), a new Mn-redox front rapidly established itself below the seafloor surface. Afterwards, this new Mn-redox front migrated constantly upwards under continuous sediment deposition until the following glacial termination (Table 5).

In line with our observations and interpretations, interstitial water profiles from ODP Sites 1095, 1096 and 1101 (Fig. 1) reveal maximum pore-water Mn-concentrations at sub-seafloor depths ranging from 12 m to 25 m (Barker et al., 1999). Above this depth, which was interpreted to correspond to the boundary between oxidising and reducing conditions (Barker et al., 1999), but more likely still lies within the suboxic zone (Kasten et al., 2004), solid-phase Mn-enrichments marking fossil Mn-redox fronts, such as those recorded in our cores, can readily be preserved.

4.4. Impact of non-steady-state diagenesis on the palaeomagnetic record

The evidence for non-steady-state diagenetic conditions affecting our cores, especially the sediments deposited around glacial terminations (section 4.3.), has implications for the palaeomagnetic records reconstructed from the sediments. Channell et al. (2019) already noted that the sediments of the JR298 cores appear unusually oxic and attributed this to low concentrations of degradable marine organic carbon. The unusually oxic conditions

promoted authigenic growth of maghemite through oxidation of detrital magnetite at the seafloor surface. The maghemite formed in the oxic zone is usually dissolved in the reducing environment, typically a few decimetres below the seabed surface in pelagic sediments, but is preserved several metres down-core in the majority of the JR298 cores (Channell et al., 2019). This down-core prevalence of maghemite was also reported from sediment records in the Arctic Ocean, and the chemical remnant magnetisation (CRM) acquired during the maghematisation process is thought to have altered palaeomagnetic recording in some of the cores (Channell and Xuan 2009; Xuan and Channell 2010; Xuan et al., 2012). The maghematisation process appears to have a debilitating effect on RPI reconstructions for cores PC723, PC727 and PC734 (Channell et al., 2019). Nevertheless, a "trial" RPI age model was proposed for core PC723, but was considered to be of poor quality. Investigations of sedimentary records from other ocean basins, including the equatorial Atlantic (e.g., Funk et al., 2004a, 2004b; Kasten et al., 2004; Reitz et al., 2004), the NW Pacific (e.g., Korff et al., 2016) and the Arctic Ocean (e.g., Wiers et al., 2019, 2020) also showed that non-steady-state diagenesis can modify the palaeomagnetic intensity and directional records through post-depositional alteration and dissolution of magnetic minerals.

We propose that (partial) alteration of the palaeomagnetic records due to non-steady state diagenesis could have led to the (predominantly minor) discrepancies between the RPI-based age models for cores PC723, PC726, PC728, PC732 and PC736 (Channell et al., 2019) and the new age models reported here (Figs. 2, 3, 5, 6 and 8; Table 3; Fig. S3a–d). There are very limited chronological constraints from the foraminiferal $\delta^{18}O$ data and the palaeoproductivity proxies for Termination I and the MIS 5/4 boundary, and positions of Termination I in the cores are largely consistent with the RPI-based age models of Channell et al. (2019) (see Fig. S3a, S3b, S3d). However, positions of Termination II in Bellingshausen Sea cores PC726 with a high quality RPI-based age model and PC723 with a poor quality RPI-based age model lie apparently deeper (by 124 and 137 cm, respectively) according to the RPI-based age models (Figs. 2 and 3; Fig. S3a). The foraminiferal $\delta^{18}O$ record of core PC726 shows a typical glacial-interglacial shift at the depth of our MIS 6/5 boundary, and a similar shift is suggested by the down-core trend of the oldest $\delta^{18}O$ data available from MIS 5 sediments in core PC723. Moreover, core PS2556, in which Marine Tephra B was clearly identified (Fig. 9; Hillenbrand et al., 2008a), can be unambiguously correlated both with core PC726 using whole-core magnetic susceptibility (Fig. S5) and with core PC723 using palaeoproductivity proxies (Figs. 2 and 9). Marine Tephra B provides a clear stratigraphic marker for Termination II, even if bioturbation and/or initial settling of the tephra on sea ice or glacial ice before its final deposition on the seabed could have resulted in a slightly time-transgressive occurrence at different core sites (Hillenbrand et al., 2008a). In addition, the RPI-based age model for core PC726 suggests the presence of MIS 7 between 945 cmcd and the core base (Channell et al., 2019). However, neither the sediment composition nor the palaeoproductivity proxies in core PC726 do support the presence of interglacial sediments in the corresponding core interval (Fig. 3). According to the correlation between cores PC726 and PS2556 (Fig. S5), MIS 7 sediments were not recovered in core PC726 because they lie deeper in the seabed, below the maximum corer penetration depth at this site. Finally, the burn-down of organic carbon during MIS 5 and MIS 7 at sites PC723 and PC726 (Figs. 2 and 3) requires sedimentation rates of <1–2 cm/kyr (Jung et al., 1997, section 4.3.). Such low sedimentation rates are in agreement with the age models proposed here but in contrast with the RPI-based age models, which yielded sedimentation rates in the order of 5–7 cm/kyr for the corresponding core intervals (Channell et al., 2019).

We attribute the age model discrepancies for the JR298 cores, i.e. mainly for the two cores from the Bellingshausen Sea, to the overprinting of the palaeomagnetic records by post-depositional diagenesis, which is clearly expressed in all three cores from the Bellingshausen Sea by major burn-down of organic carbon during interglacials MIS 5 and 7 and across Terminations II and III, respectively (Figs. 2, 3 and 9). The potential impact of non-steady-state diagenesis on RPI records may also explain the discrepancies between the original lithostratigraphy- and biostratigraphy-based age models for sediment cores from Drift 7 developed by Pudsey and Camerlenghi (1998) and Lucchi et al. (2002) and the RPI-based age models published by Sagnotti et al. (2001) and Macrì et al. (2006). Possible diagenetic overprint of the RPI record should be taken into account, when the timing of sedimentary Mn-enrichments in cores with RPI-based age models are interpreted in terms of bottom-water ventilation processes (Jimenez-Espejo et al., 2020).

Additional detailed geochemical and palaeomagnetic investigations are required to characterize the precise diagenetic overprint of the magnetic record. In the JR298 cores from the Bellingshausen Sea the stratigraphic positions of Termination II according to the RPI-based age models seem to be too deep (by ~124 and 137 cm). In the Drift 7 cores analysed by Sagnotti et al. (2001) and Macrì et al. (2006) the MIS 6/5 boundaries reconstructed from their RPI age models either match, or are also deeper than, those proposed by Pudsey and Camerlenghi (1998) and Lucchi et al. (2002), when the same sedimentological criteria are used to determine the position of this boundary (Hillenbrand et al., 2008a). It is possible that the post-depositional magnetisation lock-in process and non-steady-state diagenesis have led to delayed and (partially) altered recording of the palaeomagnetic signal. The Fe-redox front usually lies just below the Mn-redox front (e.g., Tarduno and Wilkison 1996, Kasten et al., 2004; Reitz et al., 2004; Roberts 2015). If, for example, at site PC726 the onset of highly-oxygenated bottom water flow at Termination II led to a downward oxygen diffusion and migration of the redox fronts, which may be indicated by the Mn-enrichments in the late MIS 6 sediments (Fig. 3), magnetic grains newly formed at the top of the Fe-redox front within the late MIS 6 sediments could carry a delayed chemical remanence similar to that reported in sediments from the equatorial Pacific Ocean by Tarduno and Wilkison (1996). A sudden subsequent upward shift of redox fronts in response to the interglacial productivity increase (De Lange et al., 1994; Kasten et al., 2004) or the fact, that even when the biological productivity reached its maximum, the availability of labile organic carbon was still too low to counteract the oxygen supply through the bottom water, could have allowed the preservation of the metastable element enrichments in the records.

Finally, we emphasize that below the oxic zone (i.e., ~12–25 m below the seafloor surface in our study area; Barker et al., 1999) the effect of non-steady-state diagenesis on the palaeomagnetic record should be negligible. This is confirmed by the good match between the Mid-Pleistocene (~1.6–0.7 Ma) RPI record from ODP Site 1101 (Fig. 1) and global palaeointensity stacks (Guyodo et al., 2001; Channell et al., 2019). At larger sub-seafloor depths, however, Fe-oxide dissolution in the anoxic zone and biosiliceous-rich sediments may overprint the palaeomagnetic signal, which is evident from the occurrence of magnetic susceptibility minimum zones in drill cores from the Antarctic margin (Florindo et al., 2003), including the Late Miocene to Late Pliocene sedimentary sequence from below ~80 m core depth at ODP Site 1095 (Hepp et al., 2009).

4.5. Variability of bottom current flow

We analysed $\overline{SS}$ together with SS% on cores PC727 from 2681 m water depth on Drift 7 and PC734 from 3000 m water depth on Drift 5 with the intention of reconstructing changes in bottom-current speed (Figs. 4 and 7). Whilst the correlation coefficient R between $\overline{SS}$ and SS% of samples from both cores exceeds 0.5 (section 3.2.), we do not have SS% data for all our $\overline{SS}$ data (Fig. S2). Consequently, we cannot determine the running down-core correlation R_{run} and thereby rule out poor sorting for many of our samples. This, however, is a prerequisite, if the $\overline{SS}$ data of an IRD-influenced sedimentary record are to be interpreted as a reliable proxy for bottom-current speed (McCave and Andrews 2019). Nevertheless, our $\overline{SS}$ data, which predominantly vary in a relatively narrow range between 16 and 22 μm in both cores seem to indicate only minor glacial-interglacial changes in bottom-current velocity (Figs. 4 and 7), perhaps with a slightly higher speed during interglacials and at the end of the penultimate glacial period recorded at site PC727. This result is largely in agreement with detailed grain-size data published by Pudsey and Camerlenghi (1998) from other Drift 7 cores, although in this study biosiliceous components were not removed before grain-size analysis. In general, our findings are also in line with data from core PC466 on the crest of Drift 4 (Vautravers et al., 2013). In PC466 $\overline{SS}$ fluctuates between 15 and 27 μm (average 18 μm). According to the RPI-based age model for this core, higher $\overline{SS}$ is recorded at the very end of MIS 5, which spans the lowermost part of the core (NB: only two samples from MIS 1 were analysed, which may not be representative). Vautravers et al. (2013) used a Coulter Counter MS3 only and did not separately determine SS%. However, the authors concluded, based on an anti-correlation between $\overline{SS}$ and coarse fraction content (>63 μm), a significant impact of IRD deposition on the $\overline{SS}$ record at site PC466.

Conversion of the $\overline{SS}$ data from the two JR298 cores, which were analysed with a Coulter Counter MS3, into the corresponding SediGraph grain size using the procedure proposed by McCave et al. (2017) provides full ranges of 14–19 μm for site PC727 and 13–24 μm for site PC734. According to the relation between current-meter mooring data and $\overline{SS}$ of surface sediments from the Weddell and Scotia seas obtained by McCave et al. (2017), bottom-current speed varied from 3 to 12 cm/s at site PC727 and 2 to 21 cm/s at site PC734, with a long-term average speed of 7.0 cm/s at site PC727 and 6.9 cm/s at site PC734 (Fig. S6). Such speeds are in agreement with the range of modern bottom-current velocities measured around Drift 7 (Fig. S6; Camerlenghi et al., 1997; Giorgetti et al., 2003). Bottom-current speeds exceeding ~13 cm/s are capable of winnowing some fine silt and clay particles, while erosional winnowing requires current speeds ≥20 cm/s (McCave and Hall 2006).

Bottom-current advection of fine-grained particles is evident from clay mineral assemblages in surface sediments. These assemblages show SW-ward transport of smectite-enriched detritus supplied from the South Shetland Islands along the continental rise offshore from the northern Antarctic Peninsula, and of chlorite- and illite-enriched detritus supplied from the central spine of the Antarctic Peninsula and Alexander Island along the rise offshore from the southern Antarctic Peninsula and further into the Bellingshausen Sea (Hillenbrand et al. 2003, 2005, 2009; Hillenbrand and Ehrmann 2002; Park et al., 2019). In interglacial sediments the far-travelled, distal clay mineral component is enriched with respect to the proximal component supplied from the adjacent shelf (Pudsey 2000; Hillenbrand and Ehrmann 2002; Lucchi et al., 2002), which is consistent with the clay mineral data presented here (Figs. 4, 7, 10 and 15; Table 5). Based on the indications of only weak glacial-interglacial changes in bottom-current speed on the drift crests provided by detailed grain-size data (Figs. 4 and 7; cf. Pudsey and Camerlenghi 1998), we attribute the chlorite increase in glacial-age sediments of our cores (Figs. 4, 7, 10 and 15) and other cores from the study area to a “dilution” of bottom-current transported smectite-enriched detritus (cf. Pudsey 2000; Lucchi et al., 2002; Hillenbrand and Ehrmann, 2005). This dilution was caused by an enhanced supply of glacigenic, chlorite-enriched debris from the adjacent shelf regions in response to grounded ice sheet advance during glacial periods (Ó Cofaigh et al., 2014). This hypothesis is corroborated by the sedimentation rates for our cores, which are consistently higher during a glacial period than during the preceding and subsequent interglacial period (Table 3). The increased input of glacigenic debris during glacial periods suggests that drastic reductions of palaeoproductivity proxies (Ba/Al ratios, opal and $CaCO_3$ contents) in glacial-age sediments may partially be related to dilution by terrigenous detritus.

4.6. Deposition of iceberg-rafted debris and the role of bioturbation

As it is evident from both X-radiograph observations and the down-core distributions of gravel and sand (Figs. 2–10), IRD in the sediments is mainly enriched during interglacials and at the end of glacials. In the JR298 cores, some of the sand content increase in interglacial sediments with high $CaCO_3$ content may be associated with increased planktic foraminifera abundance, because no carbonate was removed from the samples before grain-size analysis (section 2.2). However, elevated sand contents at the end of glacials and during interglacials are also recorded in cores PS1565 and PS2556 (Figs. 9 and 10), from which samples were decalcified before sieving. In core PS1565 sand-sized radiolarians probably contribute somewhat to the elevated sand content in the MIS 1 and early MIS 5 sediments (Fig. 13), but we can rule this out for core PS2556 because the radiolarian content in its sand fraction is <1.2% throughout (Braun 1997). In all cores, the sand content, and to a lesser extent the gravel content, exhibits occasionally discrete enrichments in glacial-age intervals (Figs. 2–10), a characteristic mainly caused by bottom-current winnowing and IRD supply (**Facies B** to **Facies F**, section 4.1.). The pattern of glacial-interglacial IRD deposition in our cores is consistent with previous IRD studies on the Antarctic Peninsula drifts (Pudsey and Camerlenghi 1998; Ó Cofaigh et al., 2001; Pudsey 2002; Cowan et al., 2008; Vautravers et al., 2013). High IRD supply was caused by the break-up of grounded ice masses on the adjacent West Antarctic shelf at the end of glacial periods (Hillenbrand et al., 2010; Ó Cofaigh et al., 2014) and seasonal open-water conditions during interglacial periods that allowed free drift of icebergs (Pudsey and Camerlenghi 1998; Pudsey 2000; Ó Cofaigh et al., 2001).

A surprising result of our investigation is the enrichment of gravel-sized IRD at the seafloor surfaces of the JR298 sites. With the exception of core PC727, these gravel maxima appear unprecedented when compared to the total time periods spanned by the cores, even if only those PCs which recovered sediments from previous interglacials are considered (Figs. 2–8 and 14; Figure FigS1). As for the continuous down-core gravel counts carried out on X-radiographs from GCs PS1565-2 and PS2556-2 (Figs. 9 and 10), the clast counts by Ó Cofaigh et al. (2001) and detailed grain-size analyses by Pudsey and Camerlenghi (1998) on Antarctic Peninsula drift cores, which also retrieved MIS 5 and MIS 7 sediments, did not reveal absolute maxima of coarse grains at the core-tops. Similar to GC PS1565-2, however, it is unclear whether the cores analysed by these authors retrieved (undisturbed) seafloor surface sediments, whilst no clast counts are available for the surface of MUC PS2556-1. On the other hand, we cannot rule out a sampling bias for our JR298 cores because our down-core samples

may have missed by chance gravel-rich horizons in glacial intervals (**Facies D**) and interglacial intervals (**Facies A**) that are often only visible in the X-radiographs (Fig. 16; cf. Ó Cofaigh et al., 2001).

Nevertheless, the gravel-sized IRD maximum at the surfaces of nearly all JR298 cores is such an outstanding feature that it requires further investigation. In the following, we consider four different explanations. First, the IRD maximum could result from unprecedented ice loss and associated iceberg calving from the Pacific sector of the APIS and the Bellingshausen Sea sector of the WAIS. Although major ice loss has affected both sectors over recent decades (e.g., Wouters et al., 2015; Cook et al., 2016; Christie et al., 2016; Rignot et al., 2019), we would not expect IRD supply to our sites to be higher than across glacial terminations or during MIS 5e, when marine-based parts of the WAIS are assumed to have collapsed and the APIS is assumed to have been smaller (e.g., DeConto and Pollard 2016).

Second, enhanced IRD deposition at present could be caused by warming of Southern Ocean surface waters that both increased iceberg melting and reduced seasonal sea-ice cover, allowing icebergs to drift more freely. Although overall Southern Ocean warming has been recorded over recent decades, near-surface water temperatures south of the Antarctic Polar Front have hardly warmed or actually slightly cooled (Armour et al., 2016; Swart et al., 2018), whereas sea-ice cover in our study area has decreased (e.g., Parkinson 2019). Again, however, we would not expect that current IRD deposition is higher than during MIS 5e, when surface water temperatures south of the Antarctic Polar Front were higher than today and seasonal sea-cover was reduced (e.g., Chadwick et al., 2020).

Third, the bottom current affecting the JR298 core sites could be stronger today than in the past and, thus, have enriched coarse-grained IRD by winnowing. Support for this scenario comes from the $\overline{SS}$ data in core PC734/GBC735, which reveal an absolute maximum at the seafloor surface (Fig. 7). However, we cannot rule out that this $\overline{SS}$ maximum is itself related to the high IRD content in the seafloor surface sediments (sections 3.2. and 4.5.; Fig. S2). The only other available $\overline{SS}$ data from site PC727/GBC730 seem to be less impacted by IRD deposition (sections 3.2. and 4.5.; Fig. S2), but at this site neither $\overline{SS}$ nor the gravel and sand content display absolute maxima at the surface (Fig. 4). Nevertheless, if we ignore the potential IRD caveats in our $\overline{SS}$ data (section 4.5.), the calculated maximum bottom-current speed of ~21 cm/s is reached at the surface of site PC734/GBC735 (Fig. S6). This velocity matches the maximum current speed measured in the 1990s (Giorgetti et al., 2003) and would allow some winnowing of clay and fine silt particles (McCave and Hall 2006). Strong support for the hypothesis of condensed sedimentation due to bottom-current winnowing comes from the presence of Mn-coated dropstones at the seabed surfaces of all JR298 sites (Fig. 14; Fig. S1) because the growth of Mn-coatings requires sedimentation rates $\leq$1–2 cm/kyr (e.g., Löwemark et al., 2012; Dutkiewicz et al., 2019). Given the sedimentation rates for MIS 1 (Table 3), the surface of the ~20 cm large cobble observed at site GC731/PC732 (Fig. S1) would remain exposed to Mn-precipitation from bottom water for ~8 kyr after its deposition. However, Mn-coating also affects gravel-sized IRD at the JR298 sites (Fig. 14; Fig. S1), and even very coarse gravel would have been completely buried there between 0.6 and 3.6 kyr after its deposition (Table 3). Therefore, we do not favour condensed sedimentation as explanation for the observed Mn-coating and IRD enrichment. Condensed sedimentation is also in conflict with the available average AMS ^{14}C dates of 1050 ^{14}C yrs BP and 1338 ^{14}C yrs BP obtained for seafloor surface sediments at sites GBC735/PC734 and GBC729/PC728, respectively (Table 2). These uncorrected ^{14}C ages, which also include dates on planktic foraminifera and, therefore, cannot be explained with recent colonisation of an old seafloor substrate by benthic fauna, lie within the range of the Southern Ocean MRE and thus confirm recent deposition at both core sites (section 3.4.). The data from site GBC729/PC728, where the AMS ^{14}C ages are 200–300 years older and where the concentration of coarse IRD is higher than at site GBC735/PC734 (Fig. 14), hint at only a minor degree of winnowing. Moreover, the recent AMS^{14}C ages of sand- and gravel sized (micro-)fossils from the seafloor surface at site GBC735/PC734 provide evidence that bottom-current winnowing there did not remove particles $\geq$63 μm. Independently, a recent age for the seafloor surface sediments at the studied sites is also consistent with the high TOC contents (Figs. 2–13). According to the coinciding high Ba/Al and Br/Al ratios, most of this TOC should consist of degradable, non-refractory organic material, which would have been remineralised at sedimentation rates $\leq$1–2 cm/kyr (Jung et al., 1997; Kasten et al., 2004).

The apparent conflict between the recent AMS ^{14}C dates for the seafloor surface sediments and the presence of Mn-coated dropstones leads us to a fourth explanation, i.e. the “biological upward pumping” of IRD. This process was proposed by McCave (1988) who investigated numerous box cores collected outside of the modern zone of IRD deposition on the Nova Scotia continental margin. The author observed terrigenous clasts >1–2 mm near the surface of strongly bioturbated muds in several cores, but only at sites where the mud was underlain by a diamicton (~40 cm below seafloor). McCave (1988) attributed this finding to constant upward pumping of terrigenous grains >1–2 mm from the diamicton source layer during the deposition of the overlying mud, facilitated by extensive burrowing of the sediments by detritus-feeding, infaunal organisms that were unable to ingest particles larger than sand. The author furthermore suggested that in other ocean basins biological pumping maintains Mn-nodules at the seafloor surface over (tens of) thousands of years. Piper and Fowler (1980) and Sanderson (1985) had previously highlighted the role of bioturbation in maintaining Mn-nodules at seabed surfaces.

Biological pumping would also explain the enrichment of Mn-coated, gravel-sized IRD at the surfaces of the JR298 cores (Figs. 2–8, 14; Fig. S1). As in the study of McCave (1988) the sediments near the seafloor consist of extensively bioturbated to structureless (sandy) mud (**Facies A**; section 4.1.) and were deposited at sedimentation rates ranging from 1 to 10 cm/kyr (Table 3). According to the gravel percentage data, IRD contents within or at the base of the MIS 1 sediments of the JR298 cores are very low (Figs. 2–8), but both gravel clasts observed in the X-radiographs and sand contents reveal dispersed IRD in these intervals (Fig. 16a,b). The lack of a potential distinct gravel source layer implies that the IRD has been maintained at the seabed surface since its deposition. Gravel-grain counts on X-radiographs of cores PS1565 and PS2556 (Figs. 9 and 10) and other drift cores (Ó Cofaigh et al., 2001) reveal high concentrations of gravel-sized IRD in sediments deposited from the end of MIS 2 throughout MIS 1. Such IRD-enriched sediments may provide a feasible gravel source. We speculate that the process of biological pumping may have been more active at the JR298 sites than at sites PS1565 and PS2556 and at the locations of cores analysed by Ó Cofaigh et al. (2001) because most of the JR298 cores were recovered from water depths $\leq$3000 m. Soetaert et al. (1996) and Middelburg et al. (1997) showed that the biological mixing coefficient, i.e. the degree of burrowing, is $\leq$ 1 below 3000 m, but increases exponentially with decreasing water depth. In the JR298 cores, IRD enrichments resembling those observed at the modern surface do not occur in the sediments deposited during MIS 5 or MIS 7; but with benthic activity decreasing towards the end of a (peak) interglacial in response to decreasing biological productivity, we would expect any pre-existing sharp IRD peaks to be “smeared out”.

Biological pumping may even be able to move (micro-)fossils and fossil fragments >150 μm to the seafloor surface or maintain them there over a considerable time period (McCave 1988; Thomson et al., 1995). Whilst relative maxima in sand content at the surfaces of the JR298 sites may lend some support to the hypothesis that grains <1 mm may also be affected by biological pumping, the good match between the modern Southern Ocean MRE and our AMS ^{14}C ages (section 3.4.; Table 2), which were obtained from various benthic and planktic (micro-)fossils of different sizes, do not support the hypothesis of (micro-)fossils having been "pumped upwards". In summary, however, our results indicate stratigraphic displacement of gravel-sized IRD over at least 10s of centimetres (cf. McCave 1988). This finding highlights that at core sites from water depths ≤3000 m and with low to medium sedimentation rates (~1–10 cm/kyr) caution is required in interpreting IRD records that are based on contents and/or abundances of relatively large grains (>1 mm) only.

5. Summary and conclusions

New sediment cores were recovered from the West Antarctic continental rise in the eastern Pacific sector of the Southern Ocean. Most cores, especially those targeting drift crests at ≤3000 m water depth, retrieved sediment intervals containing calcareous foraminifera, allowing AMS ^{14}C dating of surface sediments and obtaining down-core planktic foraminifera δ^{18}O records. In combination with tephrochronological constraints and lithostratigraphical down-core changes in response to glacial-interglacial cycles, the δ^{18}O data were used to establish age models for the cores. Accordingly, Late Quaternary sedimentation rates varied from ≤1 to ~20 cm/kyr and were higher during glacials.

Facies analysis confirmed previous interpretations in showing that the interplay of bottom currents with glacigenic detritus supplied from the adjacent shelf by various processes (down-slope transport, meltwater plumes, iceberg rafting) exerted the main control on sediment deposition on the rise. $\overline{SS}$ data from the drift crests suggest only minor changes in bottom-current speeds over glacial-interglacial cycles and that the current velocity changed over these timescales within the same range as over recent annual timescales. Only one instance of turbidite deposition at a shallow drift crest site was identified.

A comparison of palaeoproductivity proxies emphasizes that biogenic barium and bromine are the most reliable proxies for the supply and deposition of marine organic matter. In contrast, TOC content is affected by considerable post-depositional remineralisation and input of fossil, refractory organic matter, whilst $CaCO_3$ content is occasionally overprinted by dissolution. Biogenic opal content can be influenced by dilution by calcareous microfossils. Enrichments of solid-phase manganese at the end of glacials and during interglacials provide not only evidence for the onset of well oxygenated bottom-water conditions at glacial terminations, but also for non-steady-state diagenetic processes. "Pinning" of the redox front below the seafloor surface over prolonged time periods and possible vertical shifts of the redox front within the sediment column in response to changes in bottom-water oxygenation, biological productivity and sedimentation rates led to major burn-down of organic carbon across glacial terminations and during interglacials. This type of diagenesis probably also altered the magnetic mineralogy of the sediments and led to their delayed remanence acquisition, which may explain the differences between our new age models for the cores and previously published, RPI-based age models. Pore-water and RPI data from ODP Leg 178 cores, however, suggest that non-steady-state diagenesis mainly affects the oxic part of the sediment column. At ODP Sites 1096 and 1101 from the crests of Drift 7 and Drift 4 (Fig. 1) the base of the oxic zone was observed at sub-bottom depths of ~12–25 m, respectively (Barker et al., 1999). Given the sedimentation rates for the JR298 cores recovered from drift crests (Table 3), we can assume that at these locations sediments deposited between ~70 and 770 ka may have been affected by non-steady-state diagenesis.

Nearly all seafloor surface sediments recovered from ≤3000 m water depth on the drifts are characterized by seemingly unprecedented IRD maxima and Mn-coating of large dropstones. The required Mn-growth rates are in conflict with recent AMS ^{14}C ages on calcareous (micro-)fossils from the surface sediments. The most likely explanation for this discrepancy is upward pumping of clasts >1 mm through extensive bioturbation, which ensured the maintenance of IRD at the seabed surface throughout interglacial periods, although recently enhanced IRD supply and bottom-current winnowing were likely contributing factors. The resulting stratigraphic displacement needs to be taken into account in interpretations of IRD-records.

Data availability

All data are available under https://doi.pangaea.de/10.1594/PANGAEA.927866.

Credit author statement

C.-D. Hillenbrand: Conceptualization, Methodology, Formal analysis, Investigation, Project administration, Funding acquisition, Writing – original draft, Visualization. S.J. Crowhurst: Methodology, Formal analysis, Investigation, Resources, Writing – review & editing. M. Williams: Investigation, Writing – review & editing. D.A. Hodell: Methodology, Resources, Investigation, Funding acquisition. I.N. McCave: Methodology, Resources, Investigation, Writing – review & editing. W. Ehrmann: Resources, Investigation, Writing – review & editing. C. Xuan: Resources, Investigation, Writing – review & editing. A.M. Piotrowski: Investigation, Writing – review & editing. F.J. Hernández-Molina: Resources, Writing – review & editing. A.G.C. Graham: Resources, Funding acquisition. H. Grobe: Resources, Data curation. T.J. Williams: Investigation, Writing – review & editing. J.R. Horrocks: Investigation. C.S. Allen: Investigation. R.D. Larter: Conceptualization, Investigation, Project administration, Funding acquisition, Writing – review & editing, Visualization.

Declaration of competing interest

The authors declare that they have no known competing financial interests or personal relationships that could have appeared to influence the work reported in this paper.

Acknowledgements

We thank the Captain, officers, crew, and shipboard scientists of RRS *James Clark Ross* cruise JR298, especially J. Channell. Furthermore, we acknowledge S. MacLachlan and her team from the British Ocean Sediment Core Research Facility (BOSCORF Southampton) and V. O'Mahoney and her colleagues from The Queen's Veterinary School Hospital (University of Cambridge) for assistance with physical properties measurements and X-raying, respectively. We are grateful to J. Rolfe (University of Cambridge), S. Haessner (University of Leipzig) and M. Seebeck and R. Fröhlking (AWI) for support with laboratory analyses. N. Odling (Grant Institute, School of GeoSciences, University of Edinburgh) is acknowledged for conducting the XRF analyses on the discrete sediment samples. We also thank R. Lucchi and T. Williams for their constructive reviews,

which improved the paper. This study forms part of the British Antarctic Survey's *Polar Science for Planet Earth Programme* and was made possible by NERC UK-IODP grants NE/J006513/1 and NE/J006548/1. It has been carried out in collaboration with "The Drifters" Research Group at Royal Holloway University of London (RHUL) and is related to the TASDRACC Project funded by the Spanish Ministry of Science and Innovation (grants CTM2017-89711-C2-01-P & CTM2017-89711-C2-02-P).

Appendix A. Supplementary data

Supplementary data to this article can be found online at https://doi.org/10.1016/j.quascirev.2021.106842.

References

Armour, K.C., Marshall, J., Scott, J.R., Donohoe, A., Newsom, E.R., 2016. Southern Ocean warming delayed by circumpolar upwelling and equatorward transport. Nat. Geosci. 9, 549–554. https://doi.org/10.1038/ngeo2731.

Arndt, J.E., Schenke, H.-W., Jakobsson, M., Nitsche, F.O., Buys, G., Goleby, B., Rebesco, M., Bohoyo, F., Hong, J., Black, J., Greku, R., Udintsev, G., Barrios, F., Reynoso-Peralta, W., Taisei, M., Wigley, R., 2013. The International Bathymetric Chart of the Southern Ocean (IBCSO) Version 1.0—a new bathymetric compilation covering circum-Antarctic waters. Geophys. Res. Lett. 40, 3111–3117. https://doi.org/10.1002/grl.50413.

Barker, P.F., Camerlenghi, A., Acton, G.D., et al., 1999. In: Proceedings of the Ocean Drilling Program, Initial Reports 178. Ocean Drilling Program, Texas A&M University, College Station, TX 77845-9547, U.S.A. doi:10.2973/odp.proc.ir.178.1999.

Barker, P.F., Camerlenghi, A., Acton, G.D., Ramsay, A.T.S., et al., 2002. In: Proceedings of the Ocean Drilling Program, Scientific Results 178. Ocean Drilling Program, Texas A&M University, College Station, TX 77845-9547, U.S.A. doi:10.2973/odp.proc.sr.178.2002.

Bart, P.J., Hillenbrand, C.-D., Ehrmann, W., Iwai, M., Winter, D., Warny, S.A., 2007. Are Antarctic Peninsula Ice Sheet grounding events manifest in sedimentary cycles on the adjacent continental rise? Mar. Geol. 236, 1–13. https://doi.org/10.1016/j.margeo.2006.09.008.

Berkman, P.A., Andrews, J.T., Björck, S., Colhoun, E.A., Emslie, S.D., Goodwin, I., Hall, B.L., Hart, C.P., Hirakawa, K., Igarashi, A., Ingólfsson, O., López-Martínez, J., Lyons, W.B., Mabin, M.C.G., Quilty, P.G., Taviani, M., Yoshida, Y., 1998. Circum-Antarctic coastal environmental shifts during the Late Quaternary reflected by emerged marine deposits. Antarct. Sci. 10, 345–362. https://doi.org/10.1017/S0954102098000406.

Berkman, P.A., Forman, S.L., 1996. Pre-bomb radiocarbon and the reservoir correction for calcareous marine species in the Southern Ocean. Geophys. Res. Lett. 23, 363–366. https://doi.org/10.1029/96GL00151.

Bonn, W.J., Gingele, F.X., Grobe, H., Mackensen, A., Fütterer, D.K., 1998. Palaeoproductivity at the Antarctic continental margin: opal and barium records for the last 400 ka. Palaeogeogr. Palaeoclimatol. Palaeoecol. 139, 195–211. https://doi.org/10.1016/S0031-0182(97)00144-2.

Braun, B., 1997. Rekonstruktion glaziomariner Sedimentationsprozesse am Kontinentalrand des westlichen Bellingshausenmeeres. Diploma Thesis. Geological Institute of the University of Würzburg, Würzburg, Germany, 83 pp. (in German, with English Abstr.). hdl:10013/epic.33267.d001.

Camerlenghi, A., Crise, A., Pudsey, C.J., Accerboni, E., Laterza, R., Rebesco, M., 1997. Ten-month observation of the bottom current regime across a sediment drift of the Pacific margin of the Antarctic Peninsula. Antarct. Sci. 9, 426–433. https://doi.org/10.1017/S0954102097000552.

Chadwick, M., Allen, C.S., Sime, L.C., Hillenbrand, C.-D., 2020. Analysing the timing of peak warming and minimum winter sea-ice extent in the Southern Ocean during MIS 5e. Quat. Sci. Rev. 229, 106134. https://doi.org/10.1016/j.quascirev.2019.106134.

Channell, J.E.T., Larter, R.D., Hillenbrand, C.-D., Vautravers, M., Hodell, D.A., Hernández-Molina, F.J., Gohl, K., Rebesco, M., 2008. IODP Proposal 732-Full2: Sediment drifts off the Antarctic Peninsula and West Antarctica. Integrated Ocean Drilling Program, Texas A&M University, College Station, TX 77845-9547, U.S.A. https://docs.iodp.org/Proposal_Cover_Sheets/732-Full2_Channell_cover.pdf.

Channell, J.E.T., Xuan, C., 2009. Self-reversal and apparent magnetic excursions in Arctic sediments. Earth Planet Sci. Lett. 284, 124–131. https://doi.org/10.1016/j.epsl.2009.04.020.

Channell, J.E.T., Xuan, C., Crowhurst, S.J., Hodell, D.A., Larter, R.D., 2019. Relative paleointensity (RPI) and age control in Quaternary sediment drifts off the Antarctic Peninsula. Quat. Sci. Rev. 211, 17–33. https://doi.org/10.1016/j.quascirev.2019.03.006.

Christie, F.D.W., Bingham, R.G., Gourmelen, N., Tett, S.F.B., Muto, A., 2016. Four decade record of pervasive grounding line retreat along the Bellingshausen margin of West Antarctica. Geophys. Res. Lett. 43, 5741–5749. https://doi.org/10.1002/2016GL068972.

Cook, A.J., Holland, P.R., Meredith, M.P., Murray, T., Luckman, A., Vaughan, D.G., 2016. Ocean forcing of glacier retreat in the western Antarctic Peninsula. Science 353, 283–286. https://doi.org/10.1126/science.aae0017.

Cowan, E.A., Hillenbrand, C.-D., Hassler, L.E., Ake, M.T., 2008. Coarse-grained terrigenous sediment deposition on continental rise drifts: a record of Plio-Pleistocene glaciation on the Antarctic Peninsula. Palaeogeogr. Palaeoclimatol. Palaeoecol. 265, 275–291. https://doi.org/10.1016/j.palaeo.2008.03.010.

Cunningham, A.P., Larter, R.D., Barker, P.F., Gohl, K., Nitsche, F.-O., 2002. Tectonic evolution of the Pacific margin of Antarctica: 2. Structure of late Cretaceous-early Tertiary plate boundaries in the Bellingshausen Sea from seismic reflection and gravity data. J. Geophys. Res. 107 (B12), 2346. https://doi.org/10.1029/2002JB001897.

Davies, S.M., 2015. Cryptotephras: the revolution in correlation and precision dating. J. Quat. Sci. 30, 114–130. https://doi.org/10.1002/jqs.2766.

De Lange, G.J., Van Os, B., Pruysers, P.A., Middelburg, J.J., Castradori, D., Van Santvoort, P., Mueller, P.J., Eggenkamp, H., Prahl, F.G., 1994. Possible early diagenetic alteration of palaeo proxies. In: Zahn, R., Pedersen, T.F., Kaminski, M.A., Labeyrie, L. (Eds.), Carbon Cycling in the Glacial Ocean: Constraints on the Ocean's Role in Global Change. NATO ASI Series 17. Kluwer Academic Publishers, Dordrecht, pp. 225–258. doi:10.1007/978–3–642–78737–9_10.

DeConto, R.M., Pollard, D., 2016. Contribution of Antarctica to past and future sea-level rise. Nature 531, 591–597. https://doi.org/10.1038/nature17145.

Di Roberto, A., Colizza, E., Del Carlo, P., Petrelli, M., Finocchiaro, F., Kuhn, G., 2019. First marine cryptotephra in Antarctica found in sediments of the western Ross Sea correlates with englacial tephras and climate records. Nat. Sci. Rep. 9, 10628. https://doi.org/10.1038/s41598-019-47188-3.

Dowdeswell, J.A., Ó Cofaigh, C., Pudsey, C.J., 2004. Continental slope morphology and sedimentary processes at the mouth of an Antarctic palaeo-ice stream. Mar. Geol. 204, 203–214. https://doi.org/10.1016/S0025-3227(03)00338-4.

Dowdeswell, J.A., Ó Cofaigh, C., Noormets, R., Larter, R.D., Hillenbrand, C.-D., Benetti, S., Evans, J., Pudsey, C.J., 2008. A major trough-mouth fan on the continental margin of the Bellingshausen Sea, West Antarctica: the Belgica Fan. Mar. Geol. 252, 129–140. https://doi.org/10.1016/j.margeo.2008.03.017.

Dutkiewicz, A., Judge, A., Müller, R.D., 2019. Environmental predictors of deep-sea polymetallic nodule occurrence in the global ocean. Geology 48, 293–297. https://doi.org/10.1130/G46836.1.

Ehrmann, W., Hillenbrand, C.-D., Smith, J.A., Graham, A.G.C., Kuhn, G., Larter, R.D., 2011. Provenance changes between recent and glacial-time sediments in the Amundsen Sea embayment, West Antarctica: clay mineral assemblage evidence. Antarct. Sci. 23, 471–486. https://doi.org/10.1017/S0954102011000320.

Elderfield, H., Ferretti, P., Greaves, M., Crowhurst, S.J., McCave, I.N., Hodell, D.A., Piotrowski, A.M., 2012. Evolution of ocean temperature and ice volume through the Mid-Pleistocene Climate Transition. Science 337, 704–709. https://doi.org/10.1126/science.1221294.

Escutia, C., Bárcena, M.A., Lucchi, R.G., Romero, O., Ballegeer, A.M., Gonzalez, J.J., Harwood, D.M., 2009. Circum-antarctic warming events between 4 and 3.5 Ma recorded in marine sediments from the Prydz Bay (ODP Leg 188) and the Antarctic Peninsula (ODP Leg 178) margins. Global Planet. Change 69, 170–184. https://doi.org/10.1016/j.gloplacha.2009.09.003.

Florindo, F., Roberts, A.P., Palmer, M.R., 2003. Magnetite dissolution in siliceous sediments. Geochem. Geophys. Geosyst. 4, 379–395. https://doi.org/10.1029/2003GC000516, 1053.

Funk, J.A., von Dobeneck, T., Reitz, A., 2004a. Integrated rock magnetic and geochemical quantification of redoxomorphic iron mineral diagenesis in Late Quaternary sediments from the equatorial Atlantic. In: Wefer, G., Mulitza, S., Ratmeyer, V. (Eds.), The South Atlantic in the Late Quaternary: Reconstruction of Material Budgets and Current Systems. Springer, Berlin, Heidelberg, New York, pp. 237–260.

Funk, J.A., von Dobeneck, T., Wagner, T., Kasten, S., 2004b. Late Quaternary sedimentation and early diagenesis in the equatorial Atlantic Ocean: patterns, trends and processes deduced from rock magnetic and geochemical records. In: Wefer, G., Mulitza, S., Ratmeyer, V. (Eds.), The South Atlantic in the Late Quaternary. Reconstruction of Material Budgets and Current Systems. Springer, Berlin, Heidelberg, New York, pp. 461–497.

Gebbie, G., Peterson, C.D., Lisiecki, L.E., Spero, H.J., 2015. Global-mean marine $\delta^{13}C$ and its uncertainty in a glacial state estimate. Quat. Sci. Rev. 125, 144–159. https://doi.org/10.1016/j.quascirev.2015.08.010.

Giorgetti, G., Crise, A., Laterza, R., Perini, L., Rebesco, M., Camerlenghi, A., 2003. Water masses and bottom boundary layer dynamics above a sediment drift of the Antarctic Peninsula Pacific Margin. Antarct. Sci. 15, 537–546. https://doi.org/10.1017/S0954102003001652.

Grobe, H., 1987. A simple method for the determination of ice-rafted debris in sediment cores. Polarforschung 57, 123–126. https://doi.org/10.2312/polarforschung.57.3.123.

Grobe, H., Mackensen, A., 1992. Late Quaternary climatic cycles as recorded in sediments from the Antarctic continental margin. In: Kennett, J.P., Warnke, D.A. (Eds.), The Antarctic Paleoenvironment: a Perspective on Global Change, Antarct. Res. Ser. 56. American Geophysical Union, Washington D.C., pp. 349–376, hdl:10013/epic.11662.d001

Guyodo, Y., Acton, G.D., Brachfeld, S., Channell, J.E.T., 2001. A sedimentary paleomagnetic record of the Matuyama Chron from the western Antarctic margin (ODP Site 1101). Earth Planet Sci. Lett. 191, 61–74. https://doi.org/10.1016/S0012-821X(01)00402-2.

Hass, H.C., 2002. A method to reduce the influence of ice-rafted debris on a grain size record from northern Fram Strait, Arctic Ocean. Polar Res. 21, 299–306. https://doi.org/10.3402/polar.v21i2.6491.

Head, K.H., 2006. Manual of soil laboratory testing In: Soil Classification and Compaction Tests, third ed., vol. 1. Whittles Publishing, Caithness, UK, 412 pp.
Hennekam, R., De Lange, G., 2012. X-ray fluorescence core scanning of wet marine sediments: methods to improve quality and reproducibility of high-resolution paleoenvironmental records. Limnol Oceanogr. Methods 10, 991–1003. https://doi.org/10.4319/lom.2012.10.991.
Hepp, D.A., Mörz, T., Hensen, C., Frederichs, T., Kasten, S., Riedinger, N., Hay, W.W., 2009. A late Miocene–early Pliocene Antarctic deepwater record of repeated iron reduction events. Mar. Geol. 266, 198–211. https://doi.org/10.1016/j.margeo.2009.08.006.
Hernández-Molina, F.J., Larter, R.D., Maldonado, A., 2017. Neogene to Quaternary stratigraphic evolution of the Antarctic Peninsula, Pacific margin offshore of Adelaide Island: transitions from a non-glacial, through glacially-influenced to a fully glacial state. Global Planet. Change 156, 80–111. https://doi.org/10.1016/j.gloplacha.2017.07.002.
Hillenbrand, C.-D., 1994. Spätquaräre Sedimentationsprozesse am Kontinentalrand des nordöstliche Bellingshausenmeeres (Antarktis). Diploma Thesis. Geological Institute of the University of Würzburg, Würzburg, Germany, 124 pp. (in German, with English Abstr.).
Hillenbrand, C.-D., Cortese, G., 2006. Polar stratification: a critical view from the Southern Ocean. Palaeogeogr. Palaeoclimatol. Palaeoecol. 242, 240–252. https://doi.org/10.1016/j.palaeo.2006.06.001.
Hillenbrand, C.-D., Ehrmann, W., 2002. Distribution of clay minerals in drift sediments on the continental rise west of the Antarctic Peninsula, ODP Leg 178, Sites 1095 and 1096. In: Barker, P.F., Camerlenghi, A., Acton, G.D., Ramsay, A.T.S. (Eds.), Proc. ODP Sci. Results, vol. 178. Ocean Drilling Program, Texas A&M University, College Station, TX 77845-9547, U.S.A., pp. 1–29, doi:10.2973/odp.proc.sr.178.224.2001
Hillenbrand, C.-D., Ehrmann, W., 2005. Late Neogene to Quaternary environmental changes in the Antarctic Peninsula region: evidence from drift sediments. Global Planet. Change 45, 165–191. https://doi.org/10.1016/j.gloplacha.2004.09.006.
Hillenbrand, C.-D., Fütterer, D.K., 2002. Neogene to Quaternary deposition of opal on the continental rise west of the Antarctic Peninsula, ODP Leg 178, sites 1095, 1096 and 1101. In: Barker, P.F., Camerlenghi, A., Acton, G.D., Ramsay, A.T.S. (Eds.), Proc. ODP Sci. Results, vol. 178. Ocean Drilling Program, Texas A&M University, College Station, TX 77845-9547, U.S.A, pp. 1–33. doi: 10.2973/odp.proc.sr.178.215.2001.
Hillenbrand, C.-D., Grobe, H., Diekmann, B., Fütterer, D.K., 2003. Distribution of clay minerals and proxies for productivity in surface sediments of the Bellingshausen and Amundsen seas (West Antarctica) — relation to modern environmental conditions. Mar. Geol. 193, 253–271. https://doi.org/10.1016/S0025-3227(02)00659-X.
Hillenbrand, C.-D., Baesler, A., Grobe, H., 2005. The sedimentary record of the last glaciation in the western Bellingshausen Sea (West Antarctica): implications for the interpretation of diamictons in a polar-marine setting. Mar. Geol. 216, 191–204. https://doi.org/10.1016/j.margeo.2005.01.007.
Hillenbrand, C.-D., Moreton, S.G., Caburlotto, A., Pudsey, C.J., Lucchi, R.G., Smellie, J.L., Benetti, S., Grobe, H., Hunt, J.B., Larter, R.D., 2008a. Volcanic time-markers for Marine Isotopic Stages 6 and 5 in Southern Ocean sediments and Antarctic ice cores: implications for tephra correlations between palaeoclimatic records. Quat. Sci. Rev. 27, 518–540.
Hillenbrand, C.-D., Camerlenghi, A., Cowan, E.A., Hernández-Molina, F.J., Lucchi, R.G., Rebesco, M., Uenzelmann-Neben, G., 2008b. The present and past bottom-current flow regime around the sediment drifts on the continental rise west of the Antarctic Peninsula. Mar. Geol. 255, 55–63.
Hillenbrand, C.-D., Ehrmann, W., Larter, R.D., Benetti, S., Dowdeswell, J.A., Ó Cofaigh, C., Graham, A.G.C., Grobe, H., 2009. Clay mineral provenance of sediments in the southern Bellingshausen Sea reveals drainage changes of the West Antarctic Ice Sheet during the Late Quaternary. Mar. Geol. 265, 1–18. https://doi.org/10.1016/j.margeo.2009.06.009.
Hillenbrand, C.-D., Larter, R.D., Dowdeswell, J.A., Ehrmann, W., Ó Cofaigh, C., Benetti, S., Graham, A.G.C., Grobe, H., 2010. The sedimentary legacy of a palaeo-ice stream on the shelf of the southern Bellingshausen Sea: clues to West Antarctic glacial history during the Late Quaternary. Quat. Sci. Rev. 29, 2741–2763. https://doi.org/10.1016/j.quascirev.2010.06.028.
Huang, T.C., Watkins, N.D., Shaw, D.M., 1975. Atmospherically transported volcanic glass in deep-sea sediments: volcanism in sub-Antarctic latitudes of the South Pacific during late Pliocene and Pleistocene time. Geol. Soc. Am. Bull. 86, 1305–1315. https://doi.org/10.1130/0016-7606(1975)86<1305:ATVGID>2.0.CO;2.
Imbrie, J., Hays, J.D., Martinson, A., McIntyre, A., Mix, A.C., Morley, J.J., Pisias, N.G., Prell, W.L., Shackleton, N.J., 1984. The orbital theory of Pleistocene climate: support from a revised chronology of the marine $\delta^{18}O$ record. In: Berger, A. (Ed.), Milankovitch and Climate, Part 1. D. Reidel, Norwell, Mass, pp. 269–305. hdl:10013/epic.48655.d001.
Jaccard, S.L., Hayes, C.T., Martínez-García, A., Hodell, D.A., Anderson, R.F., Sigman, D.M., Haugh, G.H., 2013. Two modes of change in Southern Ocean productivity over the past million years. Science 339, 1419–1423. https://doi.org/10.1126/science.1227545.
Jaccard, S.L., Galbraith, E.D., Martínez-García, A., Anderson, R.F., 2016. Covariation of deep Southern Ocean oxygenation and atmospheric CO_2 through the last ice age. Nature 530, 207–210. https://doi.org/10.1038/nature16514.
Jimenez-Espejo, F.J., Presti, M., Kuhn, G., McKay, R., Crosta, X., Escutia, C., Lucchi, R.G., Tolotti, R., Yoshimura, T., Ortega Huertas, M., Macrì, P., Caburlotto, A., De Santis, L., 2020. Late Pleistocene oceanographic and depositional variations along the Wilkes Land margin (East Antarctica) reconstructed with geochemical proxies in deep-sea sediments. Global Planet. Change 184, 103045. https://doi.org/10.1016/j.gloplacha.2019.103045.
Jung, M., Ilmberger, J., Mangini, A., Emeis, K.-C., 1997. Why some Mediterranean sapropels survived burn-down (and others did not). Mar. Geol. 141, 51–60. https://doi.org/10.1016/S0025-3227(97)00031-5.
Kasten, S., Zabel, M., Heuer, V., Hensen, C., 2004. Processes and signals of non-steady-state diagenesis in deep-sea sediments and their pore waters. In: Wefer, G., Mulitza, S., Ratmeyer, V. (Eds.), The South Atlantic in the Late Quaternary. Reconstruction of Material Budgets and Current Systems. Springer, Berlin, Heidelberg, New York, pp. 431–459, doi:10.1007/978–3–642–18917–3_20.
Korff, L., von Dobeneck, T., Frederichs, T., Kasten, S., Kuhn, G., Gersonde, R., Diekmann, B., 2016. Cyclic magnetite dissolution in Pleistocene sediments of the abyssal northwest Pacific Ocean: evidence for glacial oxygen depletion and carbon trapping. Paleoceanography 31, 600–624. https://doi.org/10.1002/2015PA002882.
Kyle, P.R., Seward, D., 1984. Dispersed rhyolitic tephra from New Zealand in deep-sea sediments of the Southern Ocean. Geology 12, 487–490. https://doi.org/10.1130/0091-7613(1984)12<487:DRTFNZ>2.0.CO;2.
Larter, R.D., Cunningham, A.P., 1993. The depositional Pattern and distribution of glacial-interglacial sequences on the Antarctic Peninsula Pacific margin. Mar. Geol. 109, 203–219. https://doi.org/10.1016/0025-3227(93)90061-Y.
Larter, R.D., Hogan, K.A., Dowdeswell, D.A., 2016. Large sediment drifts on the upper continental rise west of the Antarctic Peninsula. In: Dowdeswell, J.A., Canals, M., Jakobsson, M., Todd, B.J., Dowdeswell, E.K., Hogan, K.A. (Eds.), Atlas of Submarine Glacial Landforms: Modern, Quaternary and Ancient, vol. 46. Geol. Soc. London, Memoirs, pp. 401–402, doi:10.1144/M46.132.
Lisiecki, L.E., Raymo, M.E., 2005. A Pliocene–Pleistocene stack of 57 globally distributed benthic $\delta^{18}O$ records. Paleoceanography 20, PA1003. https://doi.org/10.1029/2004PA001071.
Löwemark, L., O'Regan, M., Hanebuth, T.J.J., Jakobsson, M., 2012. Late Quaternary spatial and temporal variability in Arctic deep-sea bioturbation and its relation to Mn cycles. Palaeogeogr. Palaeoclimatol. Palaeoecol. 365, 192–208. https://doi.org/10.1016/j.palaeo.2012.09.028.
Löwemark, L., März, C., O'Regan, M., Gyllencreutz, R., 2014. Arctic Ocean Mn-stratigraphy: genesis, synthesis and interbasin correlation. Quat. Sci. Rev. 92, 97–111. https://doi.org/10.1016/j.quascirev.2013.11.018.
Lucchi, R.G., Rebesco, M., 2007. Glacial contourites on the Antarctic Peninsula margin: insight for palaeoenvironmental and palaeoclimatic conditions. In: Viana, A.R., Rebesco, M. (Eds.), Economic and Palaeoceanographic Significance of Contourite Deposits, vol. 276. Geol. Soc. London Special Publ., pp. 111–127, doi:10.1144/GSL.SP.2007.276.01.06
Lucchi, R.G., Rebesco, M., Camerlenghi, A., Busetti, M., Tomadin, L., Villa, G., Persico, D., Morigi, C., Bonci, M.C., Giorgetti, G., 2002. Mid-late Pleistocene glacimarine sedimentary processes of a high-latitude, deep-sea sediment drift (Antarctic Peninsula Pacific margin). Mar. Geol. 189, 343–370. https://doi.org/10.1016/S0025-3227(02)00470-X.
Macri, P., Sagnotti, L., Lucchi, R.G., Rebesco, M., 2006. A stacked record of relative geomagnetic paleointensity for the past 270 kyr from the western continental rise of the Antarctic Peninsula. Earth Planet Sci. Lett. 252, 162–179. https://doi.org/10.1016/j.epsl.2006.09.037.
Mangini, A., Eisenhauer, A., Walter, P., 1990. The response of manganese in the ocean to the climatic cycles in the Quaternary. Paleoceanography 5, 811–821. https://doi.org/10.1029/PA005i005p00811.
Mangini, A., Jung, M., Laukenmann, S., 2001. What do we learn from peaks of uranium and of manganese in deep sea sediments? Mar. Geol. 177, 63–78. https://doi.org/10.1016/S0025-3227(01)00124-4.
Meinhardt, A.-K., März, C., Schuth, S., Lettmann, K.A., Schnetger, B., Wolff, J.-O., Brumsack, H.-J., 2016. Diagenetic regimes in Arctic Ocean sediments: implications for sediment geochemistry and core correlation. Geochem. Cosmochim. Acta 188, 125–146. https://doi.org/10.1016/j.gca.2016.05.032.
McCave, I.N., 1988. Biological pumping upwards of the coarse fraction of deep sea sediments. J. Sediment. Petrol. 58, 148–158. https://doi.org/10.1306/212F8D3C-2B24-11D7-8648000102C1865D.
McCave, I.N., Andrews, J.T., 2019. Distinguishing current effects in sediments delivered to the ocean by ice. I. Principles, methods and examples. Quat. Sci. Rev. 212, 92–107. https://doi.org/10.1016/j.quascirev.2019.03.031.
McCave, I.N., Hall, I.R., 2006. Size sorting in marine muds: processes, pitfalls, and prospects for paleoflow-speed proxies. Geochem. Geophys. Geosyst. 7, Q10N05. https://doi.org/10.1029/2006GC001284.
McCave, I.N., Thornalley, D.J.R., Hall, I.R., 2017. Relation of sortable silt grain size to deep-sea current speeds: calibration of the 'Mud Current Meter'. Deep-Sea Res. I 127, 1–12. https://doi.org/10.1016/j.dsr.2017.07.003.
McGinnis, J.P., Hayes, D.E., Driscoll, N.W., 1997. Sedimentary processes across the continental rise of the southern Antarctic Peninsula. Mar. Geol. 141, 91–109. https://doi.org/10.1016/S0025-3227(97)00056-X.
Middelburg, J.J., Soetaert, K., Herman, P.M.J., 1997. Empirical relationships for use in global diagenetic models. Deep-Sea Res. I 44, 327–344. https://doi.org/10.1016/S0967-0637(96)00101-X.
Nitsche, F.O., Cunningham, A.P., Larter, R.D., Gohl, K., 2000. Geometry and development of glacial continental margin depositional systems in the Bellingshausen Sea. Mar. Geol. 162, 277–302. https://doi.org/10.1016/S0025-3227(99)00074-2.

Ó Cofaigh, C., Davies, B.J., Livingstone, S.J., Johnson, J.S., Smith, J.A., Hocking, E.P., Hodgson, D.A., Anderson, J.B., Bentley, M.J., Canals, M., Domack, E., Dowdeswell, J.A., Evans, J., Glasser, N.F., Hillenbrand, C.-D., Larter, R.D., Roberts, S.J., 2014. Reconstruction of ice-sheet changes in the Antarctic Peninsula since the Last Glacial Maximum. Quat. Sci. Rev. 100, 87–110. https://doi.org/10.1016/j.quascirev.2014.06.023.

Ó Cofaigh, C., Dowdeswell, J.A., Pudsey, C.J., 2001. Late Quaternary iceberg rafting along the Antarctic Peninsula continental rise and in the Weddell and Scotia seas. J. Quat. Res. 56, 308–321. https://doi.org/10.1006/qres.2001.2267.

Park, Y.K., Lee, J.I., Jung, J., Hillenbrand, C.-D., Yoo, K.-C., Kim, J., 2019. Elemental compositions of smectites reveal detailed sediment provenance changes during glacial and interglacial periods: the southern Drake Passage and Bellingshausen Sea, Antarctica. Minerals 9, 322. https://doi.org/10.3390/min9050322.

Parkinson, C.L., 2019. A 40-y record reveals gradual Antarctic sea ice increases followed by decreases at rates far exceeding the rates seen in the Arctic. Proc. Natl. Acad. Sci. Unit. States Am. 116, 14414–14423. https://doi.org/10.1073/pnas.1906556116.

Peterson, C.D., Lisiecki, L.E., Stern, J.V., 2014. Deglacial whole-ocean $\delta^{13}C$ change estimated from 480 benthic foraminiferal records. Paleoceanography 29, 549–563. https://doi.org/10.1002/2013PA002552.

Piper, D.I., Fowler, B., 1980. New constraint on the maintenance of Mn nodules at the sediment surface. Nature 286, 880–883. https://doi.org/10.1038/286880a0.

Presti, M., Barbara, L., Denis, D., Schmidt, S., De Santis, L., Crosta, X., 2011. Sediment delivery and depositional patterns off Adélie Land (East Antarctica) in relation to late Quaternary climatic cycles. Mar. Geol. 284, 96–113. https://doi.org/10.1016/j.margeo.2011.03.012.

Pudsey, C.J., 2000. Sedimentation on the continental rise west of the Antarctic Peninsula over the last three glacial cycles. Mar. Geol. 167, 313–338. https://doi.org/10.1016/S0025-3227(00)00039-6.

Pudsey, C.J., 2002. Neogene record of Antarctic Peninsula glaciation in continental rise sediments: ODP Leg 178, Site 1095. In: Barker, P.F., Camerlenghi, A., Acton, G.D., Ramsay, A.T.S. (Eds.), Proc. ODP Sci. Results, vol. 178. Ocean Drilling Program, Texas A&M University, College Station, TX 77845-9547, U.S.A, pp. 1–25, doi:10.2973/odp.proc.sr.178.214.2001.

Pudsey, C.J., Camerlenghi, A., 1998. Glacial-interglacial deposition on a sediment drift on the Pacific margin of the Antarctic Peninsula. Antarct. Sci. 10, 286–308. https://doi.org/10.1017/S0954102098000376.

Rebesco, M., Larter, R.D., Barker, P.F., Camerlenghi, A., Vanneste, L.E., 1997. The history of sedimentation on the continental rise west of the Antarctic Peninsula. In: Barker, P.F., Cooper, A. (Eds.), Geology and Seismic Stratigraphy of the Antarctic Margin: Part 2. Antarct. Res. Ser. 71. American Geophysical Union, Washington DC, pp. 29–49, doi:10.1029/AR071p0029.

Rebesco, M., Pudsey, C., Canals, M., Camerlenghi, A., Barker, P., Estrada, F., Giorgetti, A., 2002. Sediment drift and deep-sea channel systems, Antarctic Peninsula Pacific Margin. In: Stow, D.A.V., Pudsey, C.J., Howe, J.A., Faugeres, J.C., Viana, A.R. (Eds.), Deep-Water Contourite Systems: Modern Drifts and Ancient Series, Seismic and Sedimentary Characteristics, vol. 22. Geol. Soc. London Memoirs, pp. 353–371, doi:10.1144/GSL.MEM.2002.022.01.25.

Rebesco, M., Camerlenghi, A., Volpi, V., Neagu, C., Accettella, D., Lindberg, B., Cova, A., Zgur, F., the MAGICO party, 2007. Interaction of processes and importance of contourites: insights from the detailed morphology of sediment Drift 7, Antarctica. In: Viana, A.R., Rebesco, M. (Eds.), Economic and Palaeoceanographic Significance of Contourite Deposits, vol. 276. Geol. Soc. London Special Publ., pp. 95–110, doi:10.1144/GSL.SP.2007.276.01.05

Rebesco, M., Hernández-Molina, F.J., Van Rooij, D., Wåhlin, A., 2014. Contourites and associated sediments controlled by deep-water circulation processes: state of the art and future considerations. Mar. Geol. 352, 111–154. https://doi.org/10.1016/j.margeo.2014.03.011.

Reitz, A., Hensen, C., Kasten, S., Funk, J.A., de Lange, G.J., 2004. A combined geochemical and rock-magnetic investigation of a redox horizon at the last glacial/interglacial transition. Phys. Chem. Earth 29, 921–931. https://doi.org/10.1016/j.pce.2004.03.013.

Rignot, E., Mouginot, J., Scheuchl, B., van den Broeke, M., van Wessem, M.J., Morlighem, M., 2019. Four decades of Antarctic Ice Sheet mass balance from 1979-2017. Proc. Natl. Acad. Sci. U.S.A. 116, 1095–1103. https://doi.org/10.1073/pnas.1812883116.

Roberts, A.P., 2015. Magnetic mineral diagenesis. Earth Sci. Rev. 151, 1–47. https://doi.org/10.1016/j.earscirev.2015.09.010.

Sagnotti, L., Macri, P., Camerlenghi, A., Rebesco, M., 2001. Environmental magnetism of Antarctic Late Pleistocene sediments and interhemispheric correlation of climatic events. Earth Planet Sci. Lett. 192, 65–80. https://doi.org/10.1016/S0012-821X(01)00438-1.

Sanderson, B., 1985. How bioturbation supports manganese nodules at the sediment-water interface. Deep-Sea Res. 32, 1281–1285. https://doi.org/10.1016/0198-0149(85)90010-X.

Shane, P.A.R., Froggatt, P.C., 1992. Composition of widespread volcanic glass in deep-sea sediments of the Southern Pacific Ocean: an Antarctic source inferred. Bull. Volcanol. 54, 595–601. https://doi.org/10.1007/BF00569943.

Sikes, E.L., Samson, C.R., Guilderson, T.P., Howard, W.R., 2000. Old radiocarbon ages in the southwest Pacific Ocean during the last glacial period and deglaciation. Nature 405, 555–559. https://doi.org/10.1038/35014581.

Skinner, L.C., Muschitiello, F., Scrivner, A.E., 2019. Marine reservoir age variability over the last deglaciation: implications for marine carbon cycling and prospects for regional radiocarbon calibrations. Paleoceanogr. Paleoclimatol. 34, 1807–1815. https://doi.org/10.1029/2019PA003667.

Soetaert, K., Herman, P.M.J., Middelburg, J.J., de Stigter, H.S., van Weering, T.C.E., Epping, E., Helder, W., 1996. Modelling ^{210}Pb-derived mixing activity in ocean margin sediments: diffusive versus non-local mixing. J. Mar. Res. 54, 1207–1227. https://doi.org/10.1357/0022240963213808.

Stow, D., Smillie, Z., 2020. Distinguishing between deep-water sediment facies: turbidites, contourites and hemipelagites. Geosci. 10, 68. https://doi.org/10.3390/geosciences10020068.

Swart, N.C., Gille, S.T., Fyfe, J.C., Gillett, N.P., 2018. Recent Southern Ocean warming and freshening driven by greenhouse gas emissions and ozone depletion. Nat. Geosci. 11, 836–841. https://doi.org/10.1038/s41561-018-0226-1.

Tarduno, J.A., Wilkison, S.L., 1996. Non-steady state magnetic mineral reduction, chemical lock-in, and delayed remanence acquisition in pelagic sediments. Earth Planet Sci. Lett. 144, 315–326. https://doi.org/10.1016/S0012-821X(96)00174-4.

Thomson, J., Cook, G.T., Anderson, R., Mackenzie, A.B., Harkness, D.D., McCave, I.N., 1995. Radiocarbon age offsets in different-sized carbonate components of deep-sea sediments. Radiocarbon 37, 91–101. https://doi.org/10.1017/S0033822200030526.

Tjallingii, R., Röhl, U., Kölling, M., Bickert, T., 2007. Influence of the water content on X-ray fluorescence core-scanning measurements in soft marine sediments. Geochem. Geophys. Geosyst. 8, Q02004. https://doi.org/10.1029/2006GC001393.

Turney, C.S.M., Fogwill, C.J., Golledge, N.R., McKay, N.P., van Sebille, E., Jones, R.T., Etheridge, D., Rubino, M., Thornton, D.P., Davies, S.M., Bronk Ramsey, C., Thomas, Z., Bird, M.I., Munksgaard, N.C., Kohno, M., Woodward, J., Winter, K., Weyrich, L.S., Rootes, C.M., Millman, H., Albert, P.G., Rivera, A., van Ommen, T., Curran, M., Moy, A., Rahmstorf, S., Kawamura, K., Hillenbrand, C.-D., Weber, M.E., Manning, C.J., Young, C., Cooper, A., 2020. Early Last Interglacial ocean warming drove substantial ice mass loss from Antarctica. Proc. Natl. Acad. Sci. U.S.A. 117, 3996–4006. https://doi.org/10.1073/pnas.1902469117.

Vautravers, M.J., Hodell, D.A., Channell, J.E.T., Hillenbrand, C.-D., Hall, M., Smith, J.A., Larter, R.D., 2013. Palaeoenvironmental records from the West Antarctic Peninsula drift sediments over the last 75 ka. In: Hambrey, M.J., Barker, P.F., Barrett, P.J., Bowman, V., Davies, B., Smellie, J.L., Tranter, M. (Eds.), Antarctic Palaeoenviroments and Earth-Surface Processes, vol. 318. Geol. Soc. London Special Publ., pp. 263–276, doi:10.1144/SP381.12

Venuti, A., Florindo, F., Carburlotto, A., Hounslow, M.W., Hillenbrand, C.-D., Strada, E., Talarico, F.M., Cavallo, A., 2011. Late Quaternary sediments from deep-sea sediment drifts on the Antarctic Peninsula Pacific margin: climatic control on provenance of minerals. J. Geophys. Res. 116, B06104. https://doi.org/10.1029/2010JB007952.

Villa, G., Persico, D., Bonci, M.C., Lucchi, R.G., Morigi, C., Rebesco, M., 2003. Biostratigraphic characterization and Quaternary microfossil palaeoecology in sediment drifts west of the Antarctic Peninsula - implications for cyclic glacial–interglacial deposition. Palaeogeogr. Palaeoclimatol. Palaeoecol. 198, 237–263. https://doi.org/10.1016/S0031-0182(03)00403-6.

Wagner, M., Hendy, I.L., 2017. Trace metal evidence for a poorly ventilated glacial Southern Ocean. Quat. Sci. Rev. 170, 109–120. https://doi.org/10.1016/j.quascirev.2017.06.014.

Weltje, G.J., Tjallingii, R., 2008. Calibration of XRF core scanners for quantitative geochemical logging of sediment cores: theory and application. Earth Planet Sci. Lett. 274, 423–438. https://doi.org/10.1016/j.epsl.2008.07.054.

Wiers, S., Snowball, I., O'Regan, M., Almqvist, B., 2019. Late Pleistocene chronology of sediments from the Yermak Plateau and uncertainty in dating based on geomagnetic excursions. Geochem. Geophys. Geosyst. 20, 3289–3310. https://doi.org/10.1029/2018GC007920.

Wiers, S., Snowball, I., O'Regan, M., Pearce, C., Almqvist, B., 2020. The Arctic Ocean manganese cycle, an overlooked mechanism in the anomalous palaeomagnetic sedimentary record. Front. Earth Sci. 8, 75. https://doi.org/10.3389/feart.2020.00075.

Wouters, B., Martin-Español, A., Helm, V., Flament, T., van Wessem, J.M., Ligtenberg, S.R.M., van den Broeke, M.R., Bamber, J.L., 2015. Dynamic thinning of glaciers on the southern Antarctic Peninsula. Science 348, 899–903, doi:10.1126/science.aaa5727.

Wu, L., Wang, R., Xiao, W., Ge, S., Chen, Z., Krijgsman, W., 2017. Productivity-climate coupling recorded in pleistocene sediments off Prydz Bay (East Antarctica). Palaeogeogr. Palaeoclimatol. Palaeoecol. 485, 260–270. https://doi.org/10.1016/j.palaeo.2017.06.018.

Wu, L., Wang, R., Xiao, W., Krijgsman, W., Li, Q., Ge, S., Ma, T., 2018. Late Quaternary deep stratification-climate coupling in the Southern Ocean: implications for changes in abyssal carbon storage. Geochem. Geophys. Geosyst. 19, 379–395. https://doi.org/10.1002/2017GC007250.

Xuan, C., Channell, J.E.T., 2010. Origin of apparent magnetic excursions in deep-sea sediments from Mendeleev-Alpha Ridge, Arctic Ocean. Geochem. Geophys. Geosyst. 11, Q02003. https://doi.org/10.1029/2009GC002879.

Xuan, C., Channell, J.E.T., Polyak, L., Darby, D.A., 2012. Paleomagnetism of Quaternary sediments from Lomonosov Ridge and Yermak Plateau: implications for age models in the Arctic Ocean. Quat. Sci. Rev. 32, 48–63. https://doi.org/10.1016/j.quascirev.2011.11.015.

Ziegler, M., Jilbert, T., de Lange, G.J., Lourens, L.J., Reichart, G.-J., 2008. Bromine counts from XRF scanning as an estimate of the marine organic carbon content of sediment cores. Geochem. Geophys. Geosyst. 9, Q05009. https://doi.org/10.1029/2007GC001932.